Thermospheric Impact on the Magnetosphere through Ionospheric Outflow

Kevin H Pham[1], William Lotko[2], Roger Varney[3], Binzheng Zhang[4], and Jing Liu[5]

[1]National Center for Atmospheric Research
[2]Dartmouth College
[3]SRI International
[4]The University of Hong Kong
[5]High Altitude Observatory, National Center for Atmospheric Research

November 23, 2022

Abstract

We have taken a key step in evaluating the importance of ionospheric outflows relative to electrodynamic coupling in the thermosphere's impact on geospace dynamics. We isolated the thermosphere's material influence and suppressed electrodynamic feedback in whole geospace simulations by imposing a time-constant ionospheric conductance in the ionospheric Ohm's law in a coupled model that combines the multi-fluid Lyon-Fedder-Mobarry magnetosphere model with the Thermosphere Ionosphere Electrodynamic General Circulation Model and the Ionosphere Polar Wind Model that includes both polar wind and transversely accelerated ion species. Numerical experiments were conducted for different thermospheric states parameterized by F10.7 for interplanetary driving representative of the stream interaction region that swept past Earth on 27 March 2003. We demonstrate that thermosphere through its regulation of ionospheric outflows influences magnetosphere-ionosphere (MI) convection and the ion composition, symmetries, x-line perimeter and magnetic merging of the magnetosphere. Feedback to the ionosphere-thermosphere from evolving MI convection, and Alfvénic Poynting fluxes and soft (~ few 100 eV) electron precipitation originating in the magnetosphere, in turn, modify the evolving O^+ outflow properties. The simulation results identify a variety of observed magnetospheric features that are attributable directly to the thermosphere's material influence: Asymmetries in O^+ outflow fluxes and velocities in the pre/postnoon low-altitude magnetosphere, dawn/duskside lobes and pre/postmidnight plasmasheet; O^+ distribution of the plasmasheet; magnetic x-line location and reconnection rate along it. O^+ outflows during solar maximum conditions (high F10.7) tend to counteract the plasmasheet's pre/postmidnight asymmetries caused by the night-to-day gradient in ionospheric Hall conductance.

Hosted file

`essoar.10504515.1.docx` available at https://authorea.com/users/530364/articles/601835-thermospheric-impact-on-the-magnetosphere-through-ionospheric-outflow

Posted on 23 Nov 2022 — CC-BY 4.0 — https://doi.org/10.1002/essoar.10504515.1 — This a preprint and has not been peer reviewed. Data may be preliminary.

Thermospheric Impact on the Magnetosphere through Ionospheric Outflow

Kevin Pham[1], William Lotko[1,2], Roger Varney[3], Binzheng Zhang[1,4], and Jing Liu [1,†]

[1]High Altitude Observatory, National Center for Atmospheric Research, Boulder, CO, USA, [2]Thayer School of Engineering, Dartmouth College, Hanover, NH, USA, [3]Center for Geospace Studies, SRI International, Menlo Park, CA, USA, [4]Department of Earth Sciences, University of Hong Kong, Pokfulam, Hong Kong, [†]Now at Institute of Space Sciences, Shandong University, Weihai, China.

Key Points

- A global geospace model including ionospheric outflows was used to diagnose material impacts of the thermosphere on geospace
- Thermospheric states influence the distributions, fluxes and other properties of O+ outflows and their feedback on geospace dynamics
- Variations in thermospheric EUV irradiance manifest in the ion composition, shape, symmetries and magnetic merging of the magnetosphere

Abstract We have taken a key step in evaluating the importance of ionospheric outflows relative to electrodynamic coupling in the thermosphere's impact on geospace dynamics. We isolated the thermosphere's material influence and suppressed electrodynamic feedback in whole geospace simulations by imposing a time-constant ionospheric conductance in the ionospheric Ohm's law in a coupled model that combines the multi-fluid Lyon-Fedder-Mobarry magnetosphere model with the Thermosphere Ionosphere Electrodynamic General Circulation Model and the Ionosphere Polar Wind Model that includes both polar wind and transversely accelerated ion species. Numerical experiments were conducted for different thermospheric states parameterized by F10.7 for interplanetary driving representative of the stream interaction region that swept past Earth on 27 March 2003. We demonstrate that thermosphere through its regulation of ionospheric outflows influences magnetosphere-ionosphere (MI) convection and the ion composition, symmetries, x-line perimeter and magnetic merging of the magnetosphere. Feedback to the ionosphere-thermosphere from evolving MI convection, and Alfvénic Poynting fluxes and soft (~ few 100 eV) electron precipitation originating in the magnetosphere, in turn, modify the evolving O^+ outflow properties. The simulation results identify a variety of observed magnetospheric features that are attributable directly to the thermosphere's material influence: Asymmetries in O^+ outflow fluxes and velocities in the pre/postnoon low-altitude magnetosphere, dawn/duskside lobes and pre/postmidnight plasmasheet; O^+ distribution of the plasmasheet; magnetic x-line location and reconnection rate along it. O^+ outflows during solar maximum conditions (high F10.7) tend to counteract the plasmasheet's pre/postmidnight asymmetries caused by the night-to-day gradient in ionospheric Hall conductance.

Contents

1. Introduction
2. Methods
   2.1 Overview of models and coupling scheme
   2.2 Ion Outflow Acceleration
   2.3 Simulation Setup
3. Results and Discussion
   3.1 System Overview – Integrated System Parameters
   3.2 Low-Altitude System State
   3.3 Lobe Distributions
   3.4 Plasmasheet Distributions
4. Conclusions
Acknowledgements
References
Supporting Information

Correspondence
K. Pham
phamkh@ucar.edu

1. Introduction

The thermosphere exerts a significant influence on the coupled magnetosphere-ionosphere-thermosphere (MIT) system through two distinct and intertwined processes. First, it has a prominent role in determining ion-neutral drag and ionospheric conductivities (Hines, 1974; Blanc & Richmond, 1980; Brekke & Moen, 1993), which influence electrodynamic interactions such as Joule dissipation (Weiss et al., 1992), distributions of convection and electrical current (Senior & Blanc, 1984; Ridley et al., 2004; Lotko et al., 2014; Ohtani et al., 2014), subauroral polarization streams (Foster & Vo, 2002) and hemispherically integrated current-voltage relationships (Fedder & Lyon, 1987). Second, it modulates the characteristics of ionospheric ion outflows (Yau et al., 2011 and references therein), which influence the ion composition of the magnetosphere (Lennartsson et al., 2004; Kistler et al., 2005; Nose et al., 2003). Global simulations show that ion composition can change dayside and nightside reconnection rates (Brambles et al., 2010), the cross polar cap potential (Winglee et al., 2002; Welling & Zaharia, 2012), substorm dynamics (Wiltberger et al., 2010; Brambles et al., 2010; 2011; Ouellette et al., 2013; Varney et al., 2016b), plasma sheet dynamics (Garcia-Sage et al., 2015; Zhang et al., 2016a) and ring current dynamics (Glocer et al., 2009; 2018). Since all of these effects are inextricably coupled to the electrodynamics of the MIT system, it is not clear how or if the thermosphere influences the geospace system separately from its effects on ion-neutral drag and ionospheric conductivities.

Most global simulations of the MIT system effectively treat its electrodynamic interactions in isolation because ionospheric outflows are not included (Raeder, 2003; Wiltberger et al., 2004; Wang et al., 2004; Wang et al., 2008; Connor et al., 2014; Zhang et al., 2012a; 2015a; Raeder et al., 2016; Liu et al., 2018; Lin et., 2019). Global simulations including combined thermospheric influences on ion-neutral drag, ionospheric conductivities and ion outflows (Varney et al., 2016a,b; Glocer et al., 2018) to date have been based on empirical specifications of the thermosphere, e.g., using the MSIS model (Picone et al., 2002). These simulations do not include thermospheric chemistry or winds, thermospheric dynamics or feedback from the magnetosphere on the ionosphere-thermosphere.

In Review

Supporting Information

Text S1. Description of Models

Text S2. LIT Coupling Scheme and Figure S1 a schematic of the coupling scheme

Text S3. Neutral profile at the pre and post noon points of interest.

Figure S2. The solar wind parameters used to drive the simulation runs.

Figure S3. Neutral density and temperature profiles for the two points of interests marked as magenta crosses on Figure 3.

To include these effects in a geospace simulation, a physical ionospheric ion outflow model must be coupled into a global MIT simulation. We have implemented such a simulation by coupling the Ionosphere Polar Wind Model (IPWM), including effects of transverse O^+ acceleration due to wave-particle interactions (Varney et al., 2016a), into the NCAR Coupled MIT (CMIT) model (Wang et al., 2004; Wiltberger et al., 2004). The CMIT model couples the multifluid Lyon-Fedder-Mobarry (LFM) magnetohydrodynamic model for the magnetosphere and its interaction with the solar wind (Lyon et al., 2004; Wiltberger et al., 2010) to the NCAR Thermosphere-Ionosphere Electrodynamics General Circulation Model (TIEGCM). The IPWM state evolves during the simulation as the thermospheric state changes in TIEGCM. Consequently, the ionospheric ion species' mass, momentum and energy transported into the LFM computational domain by IPWM also evolve with time. The TIEGCM thermosphere and IPWM ionosphere, in turn, are both modified by the time-dependent convection electric field, electron precipitation and Alfvénic Poynting flux that LFM imposes on the ionosphere-thermosphere. Details of the coupling scheme are described in Section 2.

We isolate the nonelectrodynamic influence of the thermosphere on the magnetosphere and coupled geospace system by holding the ionospheric conductance in the MIX module constant in time. LFM uses the MIX module (Merkin & Lyon, 2010) to close its field-aligned currents at the low-altitude boundary and determine an updated convection electric field there. Imposing a constant conductance renders the thermosphere incapable of influencing the magnetospheric state when ionospheric outflows are excluded in the simulations. With a constant conductance and with ionospheric outflows included, the thermosphere has a pathway to modify the magnetospheric state by modulating outflow characteristics.

To characterize the nonelectrodynamic influence of the thermosphere on the magnetosphere, we simulated four different thermospheric states corresponding to solar minimum, solar maximum and two different intermediate solar conditions. The solar wind, interplanetary magnetic field (IMF), and solar EUV forcing of the ionosphere in IPWM are identical for all four simulations, so any difference in system characteristics are attributable solely to the differences in the thermospheric state and its influence on other elements of the geospace system. We present results from the simulations (Section 3) that illustrate, at the system level, differences in integrated system properties, as well as detailed diagnostics of differences in the IT and low- and high-altitude magnetospheric states. The paper concludes with a summary of principal results (Section 4), primary among them being that the thermosphere can have a significant influence on the magnetosphere without modulating the electrodynamics of MI coupling via changes in ionospheric conductance.

2. Methods

2.1 Overview of models and coupling scheme

The coupled model used for this study employs four components: the multifluid extension of the Lyon-Fedder-Mobarry (LFM) magnetohydrodynamic model of the magnetosphere (Wiltberger et al., 2010), the magnetosphere-ionosphere exchange (MIX) module (Merkin and Lyon, 2010) with the additional specifications for soft electron precipitation (Zhang et al., 2015b), the Thermosphere-Ionosphere-General-Circulation-Model (TIEGCM) (Wang et al., 2004; Qian et al., 2014), and the Ionosphere/Polar Wind Model (IPWM), including a causally regulated, nonthermal O^+ species (Varney et al., 2015; 2016a). A high-level overview of each model and their couplings are described below. Additional details of the models and the overall coupling scheme can be found in the Supporting Information, Figure S1 and Text S1 and S2.

LFM solves the MHD equations to 8th order on a stretched spherical grid that is densest near the Earth and bowshock and becomes coarser down tail. For these numerical experiments, the LFM runs with a grid resolution of 53 cells in the radial, 48 in azimuthal and 64 in meridional directions. The multifluid extension of the MHD equations used here solves the equations for mass continuity, momentum, and energy for four fluid species: Solar wind H^+ and three ionospheric species including H^+, thermal O^+ and "nonthermal" O^+. On the LFM upstream boundary at $x_{SM} = 30\ R_E$ the solar wind density (ρ), velocity (V_x, V_y, V_z), sound speed (c_s), and IMF (B_x, B_y, B_z) are specified in Solar-Magnetic (SM) coordinates. The ionospheric fluids are ingested into LFM's lowest altitude grid cells (at $r = 2\ R_E$) with IPWM-determined field-aligned fluxes of mass, momentum and energy. The electric field derived from the MIX ionospheric potential is also specified in the low-altitude boundary cells. Guard cells are specified so that all MHD variables satisfy Neumann boundary conditions at the low-altitude boundary, except the fluid boundary normal velocities which are set to zero.

In Review

MIX solves the Poisson equation for the electrostatic potential at 100 km altitude using LFM's field-aligned currents mapped downward along dipole field lines from the low-altitude boundary and the ionospheric conductance derived from TIEGCM. The MIX grid resolution is 2°×2° in magnetic latitude-longitude (MLAT, MLON) and extends equatorward from the pole to 46° MLAT. MIX also uses empirical relationships to specify three electron precipitation populations (Zhang et al., 2015b) used by TIEGCM and IPWM: Monoenergetic and diffuse precipitation (monodiffuse), broadband precipitation (BBE), and direct-entry cusp precipitation (cusp).

TIEGCM solves fluid equations for the major neutral species O, N_2, and O_2 and minor neutral species N and NO on a global geographic grid with 1.25°×1.25° resolution in latitude×longitude. Photoionization, dissociation, and EUV/FUV and photoelectron-impact heating rates are derived from a solar irradiance model parameterized by the F10.7 index for solar radio flux (Solomon & Qian, 2005). Precipitation-induced impact ionization and heating (Roble & Ridley, 1987; Fang et al. 2008) are calculated from the number fluxes and energies of the three populations of precipitating electrons provided by MIX. To evolve a physical thermosphere for use by IPWM, TIEGCM handles its own ion-neutral chemistry for ion species O^+, N^+, NO^+, O_2^+ and N_2^+ separately from IPWM. All species except O^+ are assumed to be in local chemical equilibrium. Ion-neutral drag leading to frictional heating (Joule heating in the neutral frame) is determined by the field-perpendicular velocity difference between major neutral species O, O_2 and N_2 and major ion species O^+, O_2^+ and NO^+ all drifting with the E×B velocity provided by MIX. TIEGCM only solves for the field-aligned transport of O^+. Its field-perpendicular transport is determined by the E×B velocity from MIX; the field-aligned transport neglects ion inertia in TIEGCM (but not in IPWM which treats higher altitudes where the ion compressibility becomes increasingly important). The TIEGCM altitude is resolved at constant pressure levels, with lowest pressure level near 97 km altitude. Depending on solar activity, the top pressure level ranges between 400 km at solar min and 800 km at solar max.

IPWM solves the eight-moment equations for the parallel transport of H^+, He^+, $O^+(^4S)$ and electrons (Varney et al., 2014). IPWM also solves the photochemistry of H^+, He^+, $O^+(^4S)$, $O^+(^2D)$, $O^+(^2P)$, N^+, NO^+, N_2^+, and O_2^+ using the reactions from Richards (2011) expanded with extra light ion reactions (Varney et al., 2014). IPWM assumes dipole magnetic field lines. Its low-latitude boundary is the surface defined by L = 4 (dipole L-shell parameter corresponding to 60° MLAT at r = 1 R_E). At its low-altitude boundary at 97 km, the IPWM grid is 2° in MLAT and 5.625° in MLON at the low-latitude boundary with decreasing MLON resolution moving inwards towards to pole to avoid excessively small cells. The IPWM grid extends from 97 km altitude up to 8000 km and expands along dipole field-lines with increasing altitude. IPWM also includes a Wave Particle Interaction (WPI) model that specifies the promotion of thermal O^+ into energetic O^+ and its transverse acceleration. For the simulation results presented here, the WPI model uses the parameters specified as run D in Varney et al. (2016b). TIEGCM provides IPWM the specification for neutral densities of the major neutral species, N_2, O_2, and O, as well as the minor neutral species NO, which is not provided by MSIS. IPWM still uses the densities of minor neutral species H, He, and $N(^4S)$, from MSIS. IPWM solves for the density of $N(^2D)$ using its own internal chemical equilibrium model. TIEGCM also provides the neutral temperature and neutral winds, which are assumed to be equal for all species. IPWM extrapolates the neutral information above the upper boundary of TIEGCM by assuming constant temperature and neutral wind in altitude, which is expected since thermal conductivity and kinematic viscosity become extremely large in the low-density limit, and by performing an exponential extrapolation of the neutral densities of N_2, O_2, NO, and O, which is the expected form in hydrostatic equilibrium at constant temperature. The exponential extrapolation uses the ratio of the TIEGCM densities between the top pressure level and the fifth pressure level from the top to estimate the scale height.

Various combinations of these models have been coupled in previous simulation studies but never all four components simultaneously. The Coupled Magnetosphere Ionosphere Thermosphere (CMIT) model, which couples LFM, MIX, and TIEGCM (e.g. Wang et al., 2008; Wiltberger et al., 2004; Wiltberger et al., 2012; Zhang et al., 2012a), has been used in numerous studies already. Varney et al. (2016a) describes an approach to couple the multifluid LFM, MIX, and IPWM to form the MFLFM-IPWM coupled model. Here we build upon these prior modeling efforts and couple all components into a single coupled model, which we refer to as the LFM-IPWM-TIEGCM (LIT) model. As an extension of the prior coupling efforts, the LIT model includes the additional coupling pathway of IPWM to dynamic thermospheric quantities from TIEGCM (where available) supplemented by MSIS, instead of using only MSIS.

In Review

In the current implementation of LIT, only one instance of IPWM is simulated representing the northern hemisphere. When coupling to MFLFM, the outflow parameters from IPWM are input into both hemispheres assuming hemispheric symmetry. The assumption of perfect hemispheric symmetry is adequate for the idealized simulations presented in this work, but future model development is needed to examine additional effects of hemispheric asymmetry.

2.2 Ion Outflow Acceleration

LFM's ideal MHD model only treats isotropic fluids, and thus cannot treat the magnetic mirror force above r = 2 R_E. IPWM's anisotropic, nonthermal O^+ fluid is converted to an isotropic bulk fluid when its fluxes are ingested in LFM's low-altitude boundary cells. In the treatment in Varney et al. (2016a), the mirror force above LFM's low-altitude boundary was completely ignored. For this work we have revised this procedure to generate parallel velocities that are closer to observations (e.g. Bouhram et al. 2004). To model continued evolution of the anisotropic nonthermal O^+ fluid above LFM's low-altitude boundary before its moment fluxes are ingested into LFM's low-altitude boundary cell, we first perform an adiabatic mapping along dipole field lines of the anisotropic velocity ($v_{\parallel 0}, v_{\perp 0}$) of the nonthermal O^+ in IPWM at the inner boundary of LFM to a reference radial distance r_{ref}. The parallel velocity $v_{\parallel 0}$ is calculated directly by the IPWM parallel momentum equation. The perpendicular velocity $v_{\perp 0} \equiv \sqrt{2\,p_{\perp 0}/mn_0}$ is derived from the IPWM solution for the perpendicular pressure $p_{\perp 0}$ and number density n_0. The mapping conserves the first adiabatic invariant ${v_\perp}^2/B$, kinetic energy $½m\left(v_\parallel^2 + v_\perp^2\right)$, and number flux $nv_{||}$ of the nonthermal O^+. After determining the mapped values, we then 1) assign the mapped $v_\parallel$ to the parallel bulk velocity of the nonthermal O^+ ingested in LFM's boundary cells and 2) from the mapped $v_\perp$, assign $½mv_\perp^2$ to the *isotropic* temperature of the ingested nonthermal O^+. The number density of the ingested nonthermal O^+ is reduced such that the number flux remains unchanged as a result of the mapping.

We have chosen $r_{ref} = 6\ R_E$ for the mapping since the above procedure results in a temperature of about 10-30 eV at ingestion at LFM's low-altitude boundary at $r = 2\ R_E$ and $v_\parallel$ values ranging approximately from 30-70 km/s, which are comparable to Cluster measurements (Bouhram et al., 2004). The MHD equations impart an additional centrifugal acceleration to its upward flowing fluids above the low-altitude boundary owing to the action of convection on the parallel streaming fluid.

This adiabatic mapping procedure does not capture any additional nonadiabatic acceleration that may be occurring due to wave-particle interactions above the altitude limits of the IPWM domain. Cluster satellite data indicate that O^+ undergoes wave-particle interactions and continuous energization in the cusp up to about r = 3.5 R_E before asymptotically reaching a parallel velocity ($v_{||}$) ranging from 40 km/s to 200 km/s and a temperature ranging from 80 eV to 2000 eV (Bouhram et al., 2004). Including additional nonadiabatic acceleration in the LFM domain will require future model development.

We found that ion outflows entering the LFM domain with subsonic velocities usually do not leave LFM's lower altitude grid cells. When this occurs, the fluid accumulates near the low-altitude boundary, and the fluid density becomes unrealistically large, which is especially problematic for the long-duration simulations of this paper. To remedy the problem, each IPWM fluid is only ingested in an LFM boundary cell when its mapped parallel velocity is supersonic.

2.3 Simulation Setup

The idealized numerical experiments in this study use realistic solar wind inputs based on an interplanetary stream interaction region (SIR) that swept past Earth on 26-27 March 2003 (Jian et al., 2006). The variability in IMF and dynamic pressure typically associated with an SIR stimulates Alfvénic Poynting fluxes flowing into the cusp, and such events can be expected to produce relatively prodigious cusp O^+ outflows. Additionally, the periods of moderately intense southward IMF in the chosen SIR event produce magnetotail activity that also stimulates earthward-directed Alfvénic Poynting fluxes and O^+ outflows on the nightside. Thus SIR events are ideal candidates for numerical experiments to study the effects of ionospheric outflows on geospace dynamics. The variability in ρ_{SW} and IMF B_z in this event are sufficient to generate significant Alfvénic power flowing to low altitude, so we chose to simplify the inputs by setting the other solar wind velocity components (V_y, V_z) and IMF components (B_x, B_y) to zero. This study uses controlled, idealized numerical experiments to

In Review

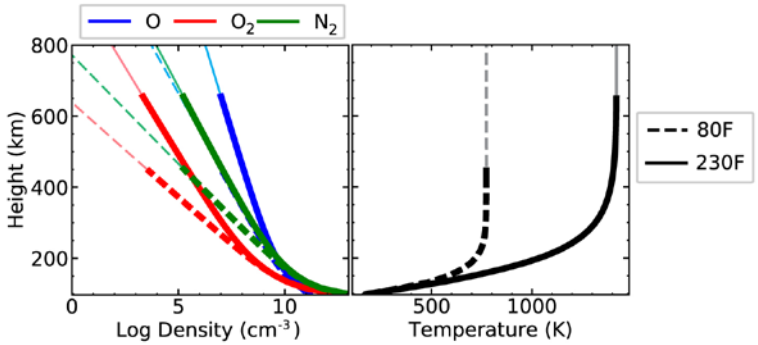


Figure 1. Altitude profiles of the O (blue), O2 (red) and N2 (green) density (left) and composite temperature (right) averaged over the northern hemispheric MLAT-MLON domain of IPWM at 1600 UT on 26 March 2003 for F10.7 inputs of 80 SFU (dashed) and 230 SFU (solid). Dark portion of each curve is determined directly by TIEGCM. IPWM's extrapolation to altitudes above TIEGCM's domain is indicated by the light extension of each curve.

isolate cause and effect rather exacting simulations of the 26 March 2003 event. Nonzero IMF $B_{x,y}$, in particular, can introduce externally imposed hemispheric and dawn-dusk asymmetries in the geospace response that masks asymmetries produced by internal processes. Figure S2 of the Supporting Information provides a plot of the solar wind and IMF parameters used for this study.

To examine the thermospheric influence on geospace dynamics via ionospheric ion outflows, we vary one of the major sources of thermospheric variability in the TIEGCM simulations, the solar EUV flux. The solar irradiance controls (Hedin & Mayr, 1987): 1) direct heating of the thermosphere, which influences the scale heights of the neutral total density and temperature, and 2) ionization of the thermosphere, which determines the altitude profiles of the electron density, Pedersen conductivity, and Joule heating of the thermosphere. The proxy input to the modified EUVAC model that specifies the solar EUV flux in TIEGCM (Solomon & Qian, 2005) is the daily F10.7 index, a measure of the solar radio flux at 10.7 cm.

Four different TIEGCM states were simulated corresponding to F10.7 values of 80 SFU, 130 SFU, 180 SFU, and 230 SFU (designated 80F, 130F, 180F, and 230F runs). Diagnostic results are presented here only for the extreme cases, 80F and 230F, but we determined that thermospheres corresponding to intermediate F10.7 produced intermediate results for each diagnostic. The 80F and 230F runs can be considered as representative of solar minimum and solar maximum states. Altitude profiles of the densities and temperatures for the major neutral species O, O_2, and N_2 averaged over the IPWM spatial domain in MLAT-MLON for the two extremes (80F and 230F) are shown in Figure 1 at 1600 UT on 26 March 2003 when the LIT component models are first coupled. When F10.7 was increased from 80 SFU to 230 SFU, the thermospheric densities and temperature increased.

In order to isolate the effects of the changes in the thermospheric state from solar EUV effects on ionospheric chemistry and electron heating, we specified the same value of F10.7 (180 SFU) in the IPWM input for all four runs. IPWM uses F10.7 in two ways: 1) as input to its irradiance model, which is used to determine photoionization and photoelectron heating, and 2) as input to the MSIS thermosphere, which is used to specify characteristics of the minor species not taken from TIEGCM. Using the same F10.7 input to IPWM for all runs maintains the same irradiance for photoionization and further isolates variations in the thermospheric influence on geospace dynamics. All models are preconditioned using standard procedures for each individual model, as described in Text S3 of the Supporting Information.

With the integration of IPWM into CMIT and its causally regulated ionospheric outflows, the TIEGCM thermosphere has two pathways to impact the geospace system: 1) It determines the ionospheric conductivity which influences MIT electrodynamics; and 2) It modulates the composition and scale height of the neutral atmosphere and, therefore, the source densities and fluxes of ionospheric ion outflows, which influence mass loading of the magnetosphere and MIT coupling and feedback. To isolate the outflow effects in the LIT model, we used time-constant ionospheric conductances in MIX so that the magnetosphere always sees the same conductance for runs with different thermospheric states. The static conductance in MIX includes the EUV conductance distribution described by Wiltberger et al. (2009) for an F10.7 of 180 SFU and a 2 S floor on both the Pedersen and Hall conductance throughout the MIX grid. LFM does not see the electron precipitation-induced conductances that the standard MIX module calculates.

3. Results and Discussion

3.1 System Overview – Integrated System Parameters

The impact of different thermospheric states (e.g., Figure 1) on geospace dynamics can be characterized by a variety of diagnostics. In this subsection we present an overview based on time series of key integrated (lumped) system parameters. Figure 2 shows time series of the hemispherically integrated outflow rate calculated at the inner boundary of LFM, cross polar cap potential (CPCP) and the difference in CPCP between runs (80F minus 230F). A 30-minute moving mean has been applied to each curve in Figure 2. The yellow band in Figure 2 from 0600-1200UT on 27 Mar 2003 delineates the interval during which six-hour average states are calculated for various diagnostic quantities discussed in subsequent analysis. It is a period of moderate interplanetary driving as measured by the average IMF B_z = –5.3 nT (cf. SI Figure S2).

The average CPCP during this interval is 162kV and 156kV for the 80F and 230F runs, respectively. The average reduction in the CPCP between the 230F and 80F runs is relatively small, but it can be as large as 20 kV over limited durations near peaks in the CPCP (Figure 2, bottom) and can even reverse sign. As noted previously (Winglee et al., 2002; Brambles et al., 2010; Welling & Zaharia, 2012), the CPCP is usually lower when the magnetosphere is loaded with more O^+, the likely cause being the effect of O^+ in lowering the magnetopause reconnection rate (Lotko, 2007). We return to this point in Sec. 3.4 where dayside reconnection rates and potentials are determined. In both runs the CPCP (Figure 2, middle) tends to decrease as the O^+ outflow rate (Figure 2, top) increases, but the trend is not universal due to partial masking by application of a moving mean combined with the more latent response to solar wind variability of the outflow rate relative to the CPCP. The generation and timing of cusp-region Alfvénic Poynting flux is similar in both runs owing to the driven nature of the magnetosphere and the same solar wind driving in both runs. Consequently, the timing of O^+ energization, which is causally regulated in the outflow model by Alfvénic Poynting flux, is accompanied by similar timings of enhanced outflow in the two runs.

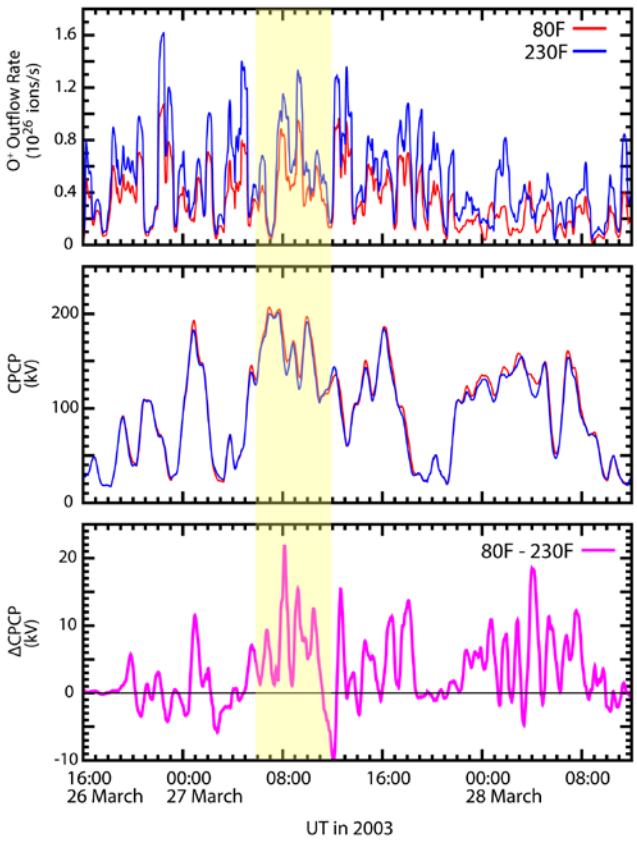


Figure 2. Outflow rate of energetic O^+ integrated over the northern hemisphere (top), the CPCP (middle) and the difference in CPCP for 80F run minus 230F run (bottom) versus UT. A 30-minute moving mean has been applied to each curve. The yellow band is a 6-hour period of moderately elevated solar wind activity and CPCP during which a six-hour average state is used in subsequent analysis.

Table 1 compares the relative effects of six-hour average 80F and 230F thermospheric states for the integrated O^+ outflow flux F_{O^+}; average O^+ outflow velocity $\bar{V}_{\parallel O^+}$; and integrated downflowing Alfvénic Poynting flux $S_\parallel$. $\bar{V}_{\parallel O^+}$ is calculated by first integrating the momentum flux over the surface of interest (dayside or nightside) and then averaging the result over the six-hour interval. The number flux is integrated over the same surface area and averaged over time. The integrated momentum flux divided by the integrated number flux produces the average outflow velocity $\bar{V}_{\parallel O^+}$. The numerical values in Table 1 are split into the northern hemisphere's dayside and nightside, which we delineate by integrating and averaging sunward and antisunward of the dawn-dusk meridian, respectively. The percent difference, Δ%, is calculated for any variable A as $(A_{230F}/A_{80F} - 1) * 100$.

The hemispherically integrated flux of

	80F, day	230F, day	Δ_{day} %	80F, night	230F, night	Δ_{night} %
F_{O^+}, 10^{25} ions/s	2.8	3.8	36	1.5	2.4	60
$\bar{V}_{\parallel O^+}$, km/s	32	33	3	45	38	−16
$S_\parallel$, GW	0.22	0.22	0	0.33	0.22	−33

Table 1. Six-hour average values for the interval 0600-1200 UT on 27 March. The downflowing Alfvénic Poynting flux ($S_\parallel$) and energetic O^+ outflow flux (F_{O^+}) are integrated over dayside and nightside areas. The O^+ outflow velocity ($\bar{V}_{\parallel O^+}$) is an average over dayside and nightside areas. Δ% is the percent difference of the 230F variable relative to the 80F variable.

nonthermal O^+ flowing into the LFM domain from IPWM (Figure 2, top) is nearly always greater for the 230F run than the 80F run, with six-hour averages from 0600-1200 UT on 27 Mar exhibiting a 36% increase in the outflow rate in Table 1 on the dayside and a 60% increase on the nightside. The outflow rates for low and high F10.7 are comparable to those reported by Yau et al. (2013) based on ion measurements from the Dynamics Explorer-1 (DE-1) satellite. Their empirical regression formula for the F10.7 dependence of the O^+ outflow rate, $F_{O^+} \propto \exp(10^{-2}F_{10.7})$, gives a predicted increase of ≈ 350% at 230 SFU relative to 80 SFU at the relatively high Kp values (4⁻ to 5⁻) of our six-hour averaging interval, but their regression formula is least accurate at high Kp and extreme F10.7 (their Fig. 2). The simulated increase in hemispheric outflow rate with increasing F10.7 is significantly less (44%) than that predicted by Yau et al.'s empirical formula, but the simulations were designed to isolate the effects of changes in the distribution, composition, density, temperature and wind of thermospheric *major* neutral species from all the other effects of solar EUV. In contrast, the empirical predictions are derived from observations that mix together all of the effects of solar EUV on the system. The solar EUV production and photoelectron heating in IPWM, the neutral H density that affects charge exchange, and the ionospheric conductance are all held constant between the runs. Even with the solar EUV in IPWM held constant, the higher thermospheric neutral densities and temperatures in the 230F run lead to higher rates of topside O^+ production. This result was anticipated by Cannata and Gombosi (1989) who concluded that an increase in atomic oxygen density during solar maximum leads to an increase in O^+ in the topside ionosphere and exosphere during solar maximum.

This simulated dependence of $\bar{V}_{\parallel O^+}$ on F10.7 is consistent with the observed dependence reported by Abe et al. (2004). Despite the 230F run's reduced acceleration and slower $\bar{V}_{\parallel O^+}$, its outflow rate is still higher relative to the 80F run because the 230F thermosphere produces a higher O^+ source density available for energization and outflow. This effect evidently overcompensates the reduction in outflow velocity.

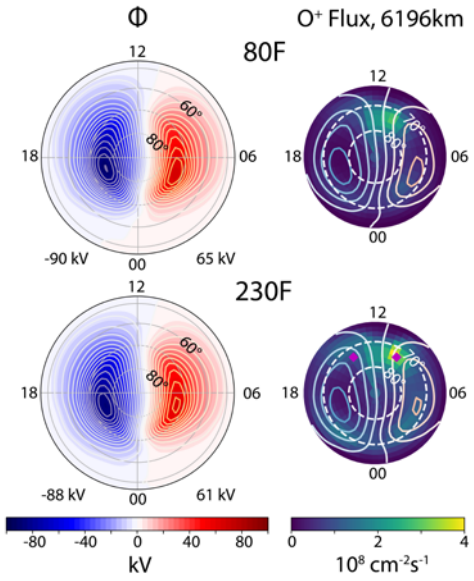


Figure 3. Ionospheric potential (left) and O^+ outflow flux distributions at 6196 km altitude (right) vs MLT and MLAT, time-averaged from 06-12 UT on 27 March. The contours in all plots correspond to electric potential. Values below each potential plot give the minimum and maximum potentials. The magenta squares denote postnoon (10 UT) and prenoon (14 UT) regions of interest at 74° MLAT.

3.2 Low-Altitude System State

We now consider low-altitude distributions of select state variables averaged over the nominal six-hour interval (0600-1200 UT, 27 Mar 2003). The average ionospheric potential distributions shown in Figure 3 (left) are similar for the two runs, albeit with a cross polar cap potential 4% larger magnitude in the 80F than in the 230F run. Since the MIX ionospheric conductances are the same in the two runs, this difference in CPCP must be due to commensurately different reconnection potentials at the dayside magnetopause (to be discussed in Sec. 3.4). The transpolar potential distributions in both runs indicate that more magnetic flux circulates in the dusk cell than in the dawn cell, with 60% of the total flux circulating in the dusk cell. This asymmetry is a consequence of the day-to-night Hall conductance gradient resulting from the EUV-induced ionization and conductance (Lotko et al., 2014). Since the MIX conductance distribution is the same in both runs, it is not

In Review

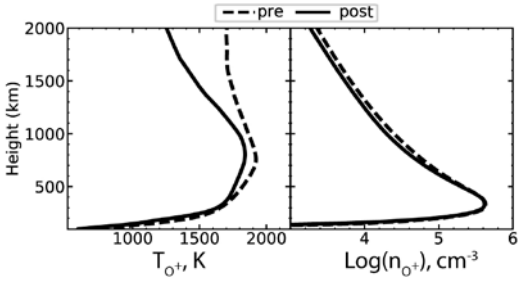


Figure 4. Six-hour time-average (from 06-12 UT on 27 March) thermal plus energetic O^+ temperature (left) and density (right) vs altitude for the prenoon and postnoon points marked as magenta squares in Fig. 3 (230F run).

surprising that the degree of asymmetry in the potential distributions is the same.

The distribution of energetic O^+ outflow flux (Figure 3, right) at 6196 km altitude, where the IPWM O^+ flux enters the LFM domain, is higher on the dawn side than on the dusk side. This asymmetry cannot be externally imposed because the solar wind/IMF variables (ρ, V_x, B_z) driving the simulation produce neither a dawn/dusk nor a hemispheric asymmetry. It must arise from something inherent in the system. A prenoon enhancement in outflow flux in the low-altitude upflowing flux of O^+ and in the high-altitude outflow flux has been reported in many observational studies using ground-based radars (Evans, 1975) and satellite data from DE-1 (Lockwood et al., 1985; Pollock et al., 1990; Giles et al., 1994), Polar (Lennartsson et al., 2004), DMSP (Redmon et al., 2012), FAST (Andersson et al., 2005) and Cluster (Liao et al., 2010). The extensive altitude range of these observations indicate that the prenoon enhancement in outflow flux persists from low altitudes in the topside ionosphere up to high altitudes in the cusp and lobes. While the feature is evidently common, its causality has yet to be fully resolved. Based on quiet-time, ionospheric simulations using the FLIP model, Redmon et al. (2012) attribute the asymmetry primarily to a rise in upward O^+ flux after sunrise caused by solar illumination-induced thermal expansion. As the plasma moves eastward toward noon and beyond, it approaches equilibrium along the flux tube in the simulations, reducing the temperature gradient and upward flux. Liao et al. (2010) attributed the asymmetry of O^+ outflows observed in the lobes to an asymmetry in convection caused by the effect of the night-to-day gradient on ionospheric conductivity. The LIT simulations treat all of the processes described in these studies in concert with IPWM's O^+ WPI energization mechanism, and we next diagnose features of the prenoon enhancement in the LIT ionosphere-thermosphere and magnetosphere.

The prenoon enhancement is most prominent in the 230F run, so we analyzed it in detail. Prenoon (10 MLT) and postnoon (14 MLT) points of interest located at 74° MLAT are marked as magenta squares in Figure 3 (bottom right). The height profiles of the O^+ temperature and density at the two fiducial points are shown in Figure 4. Contributions from both the thermal and transversely accelerated O^+ are included in the plot, but only the thermal species contributes below 600 km altitude. The temperatures in Figure 4 start to diverge near 300 km altitude. A potential cause of this asymmetry is the magnetosphere. LFM's empirical model for BBE precipitating number flux exhibits a prenoon enhancement (Figure 5, left) consistent with the prenoon enhancement in topside O^+ upflow. The prenoon enhancement in BBE precipitation is also shifted poleward relative to the postnoon enhancement (peak near 74° vs 70° MLAT). In addition, the dawnward shift in the convection throat in Figure 3 (evidenced by the location of the zero-potential contour) causes direct-entry cusp electron precipitation to exhibit the same prenoon enhancement. With typical energies of ~ 400eV, BBE and direct-entry cusp electron precipitation deposit energy in the ionosphere-thermosphere near 300 km altitude, augment the Pedersen conductivity of the bottomside *F* region, and stimulate IT heating and upwelling above that altitude (Zhang et al., 2012a). This effect contributes to the asymmetry in the ion temperature, and together with increased O^+ production due to the increase in neutral O scale height in the 230F run (Figure S3), to the enhancement in topside O^+ density in Figure 4 (right). At 1000 km altitude at the fiducial points in Figure 3, the prenoon O^+ density is 26% (51%) greater in the 230F (80F) run than the postnoon density.

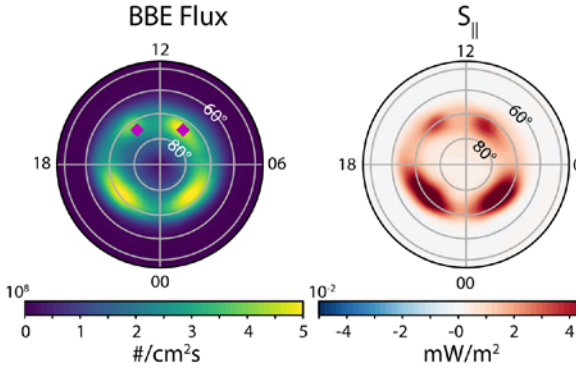


Figure 5. Six-hour time-average (over 06-12 UT on 27 March) distributions of BBE precipitating number flux (left) and Alfvénic Poynting flux (right) mapped to 100km vs MLT and MLAT in the 230F LIT run.

In Review

The downflowing Alfvénic Poynting flux $S_{||}$ extracted from LFM exhibits the same MLT/MLAT pattern as the BBE precipitation (Figure 5, right), as it should because the precipitating BBE flux is parameterized in MIX as a power-law function of Aflvénic $S_{||}$ (Zhang et al., 2015b). Since the downflowing Alfvénic Poynting flux additionally regulates O^+ energization in IPWM's WPI model, its pre/postnoon asymmetry introduces asymmetry in the O^+ outflow independently of the thermosphere, at least in the current implementation of LIT. Direct Alfvénic Joule heating of the thermosphere, which is not included here, can also augment neutral upwelling. The analysis thus far does not determine relationships between these parameters nor does it determine the primary causality of the pre/postnoon asymmetry. A more in-depth analysis is certainly warranted.

3.3 Lobe Distributions

The previous analysis shows that IPWM ingests O^+ outflow into LIT's low-altitude magnetosphere predominantly in the prenoon sector. This asymmetry persists in the lobes. Figure 6 shows the field-aligned flux of the energetic O^+ in color in a Y_{SM}–Z_{SM} plane at X_{SM} = –15 R_E, averaged over the same 6-hour interval indicated in Figure 2 and Table 1. The prenoon/dawnward (Y_{SM} < 0) shift in the O^+ flux is clearly present near the Y_{SM} axis, although it is less conspicuous than at low altitude. Positive (red) in Figure 6 indicates parallel to the magnetic field. As expected the flow is tailward everywhere outside the black closed contour, which is the field line mapping onto the Y–Z plane of the last closed field line in the plasma sheet (inferred on Z_{SM} = 0 plane). It separates closed plasmasheet field lines (within black contour) in this projection from open lobe field lines (outside black contour). Regions of sunward-directed field-aligned flux, several R_E wide in Y_{SM}, occur within the black contour. These are (6-hour) time-average projections of O^+ fluxes entrained in the plasmasheet flow channels (bursty bulk flows) seen in Cluster data (Nakamura et al., 2004) and previous LFM simulations (Wiltberger et al., 2015; Merkin et al., 2019). The fact that they are more prominent on the dusk side than the dawn side is discussed in Sec. 3.4 where plasmasheet diagnostics are presented. The white squares in Figure 6 give an impression of the magnetopause location in this plane and are points where solar wind streamlines intersect the Y–Z plane.

The green vectors in Figure 6 represent the local field-perpendicular velocity ($\boldsymbol{E} \times \boldsymbol{B}$) projected onto the Y–Z plane from the simulated polar cap. As expected for the dawn-to-dusk electric field in the simulated polar cap (Figure 3, left), the $\boldsymbol{E} \times \boldsymbol{B}$ drift transports the fluid predominantly toward the plasmasheet in the lobes; however, it also has a duskward component in this projection. The duskward drift is not imposed by the solar wind (V_x only) or IMF (B_z only) and is a consequence of the sunward gradient in ionospheric Hall conductance (Lotko et al., 2014). It is energetically more favorable for the ionosphere to polarize in response to a divergent Hall current than to work against the high Alfvén impedance to field-aligned current flow, the alternative pathway for alleviating a Hall-current divergence. The polarization produces a secondary, sunward-directed electric field and the duskward $\boldsymbol{E} \times \boldsymbol{B}$ drift apparent in the lobes. Since Figure 6 is a 6-hour average, the $\boldsymbol{E} \times \boldsymbol{B}$ vectors do not vanish at the open-closed boundary (black curve) or become tangential there, as they should because the MHD flow is ideal on either side of the boundary and cannot cross the magnetic separatrix without magnetic reconnection. Reconnection occurs near the magnetic equator in the plasmasheet, not the lobes. The instantaneous flow is ideal on either side of the instantaneous boundary, but plotting *average* $\boldsymbol{E} \times \boldsymbol{B}$ flow vectors makes it

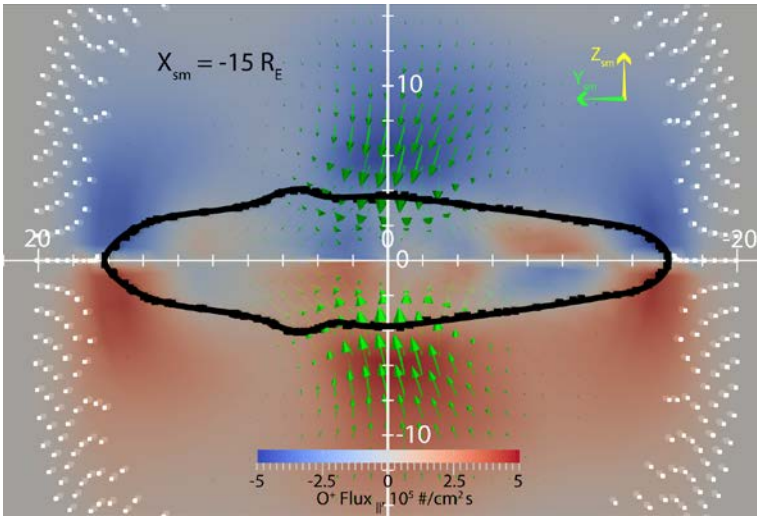


Figure 6. Six-hour time-average (over 06-12 UT on 27 March) field-aligned flux of the energetic O^+ (color scale) in a Y_{SM}–Z_{SM} plane at X_{SM} = –15 R_E for the 230F run. Positive (red) is parallel to the magnetic field. The green arrows are $\boldsymbol{E} \times \boldsymbol{B}$ velocity vectors projected onto the plane. The black contour is the projection along magnetic field lines of the last closed field line in the Z_{SM} = 0 plane. The white points are the intersection of solar wind streamlines with this plane.

In Review

appear nonideal at the *average* boundary location.

The occurrence frequency of streaming O^+ in Cluster CODIF measurements integrated from $-20\ R_E < X_{GSM} < -5\ R_E$ in the lobes exhibits a similar dawnward shift in the northern lobe, even when all IMF clock angles are included in the statistics (Liao et al., 2010). However, the asymmetry shifts duskward in the southern lobe. The cause of the shift is not clear. Season may be a factor because in Liao et al.'s 2010 study Cluster was in the northern/southern hemisphere during summer/winter, respectively. Solar cycle phase may also be a factor which, as demonstrated in Sec. 3.2, changes the underlying thermospheric state and its influence on O^+ outflow. The data in the Liao et al. (2010) study was acquired in 2001-2002 at solar maximum. The occurrence frequency of streaming, cusp-origin O^+ exhibits a predominant dawnward shift in 2003 (the year of the SIR event simulated here) in both the north and south (Liao et al., 2012), though it is not hemispherically symmetric as in Figure 6. Proper hemispheric symmetry/antisymmetry is not treated in the currently implemented LIT model, because the IPWM ionosphere and outflowing O^+ are required to be hemispherically symmetric by construction. Additional LIT model development is needed to address the hemispheric asymmetries reported by Liao et al.

3.4 Plasmasheet Distributions

The O^+ density distributions in the simulated equatorial plane ($Z_{SM} = 0$) for the 80F and 230F runs, time-averaged over the same six-hour active period as in prior figures, are shown in color in Figure 7. The white contours delineate the average $B_z = 0$ contour in each run—essentially the average magnetic x-line for the solar wind/IMF driving conditions in these simulations with no dipole tilt (Ouellette et al., 2010). The dayside density depletion in the plots located within the magnetosphere and sunward of the low-altitude simulation boundary at $r = 2\ R_E$ is an artifact of the simulation. The simulation model does not include corotation or gradient-curvature drifts, and the $\boldsymbol{E} \times \boldsymbol{B}$ convection paths do not reach the shadow region sunward of the low-altitude simulation boundary before undergoing reconnection at the dayside magnetopause.

Given the greater low-altitude O^+ outflow flux in the 230F run than in the 80 F run, it is not suprising that the plasmasheet in Figure 7 contains more O^+ in the 230F run than the 80F run. This F10.7 dependence of the simulated O^+ density is consistent with satellite observations in the midtail plasmasheet ($-15 < X_{SM} < -20\ R_E$) plasmasheet (Lennartsson, 1989; Mouikis et al. 2010; Maggiolo & Kistler, 2014). The average simulated O^+ densities are within the range reported by Maggiolo & Kistler (their Figure 2) for the magnetic activity level (Kp = 4-5) of the six-hour averaging window (06-12 UT 27 March 2003). The simulations exhibit a weak asymmetry in the O^+ density of the midtail plasmasheet (-15 to $-20\ R_E$) with about 10% greater post-midnight density within ± 2 hours MLT (Y_{GSM} within $\pm 10\ R_E$) of midnight. The Cluster CODIF measurements present a somehwat mixed picture of this asymmetry in midtail O^+ density (Mouikis et al. 2010; Maggiolo and Kistler, 2014) with large error bars on the distributions.

The shape of the simulated plasmasheet inferred from the x-line perimeter in Figure 7 is noticeably asymmetric across midnight in the 80F run and slightly asymmetric in the 230F run, with the plasmasheet contracted on the post-midnight side relative to pre-midnight. This asymmetry is due to the sunward gradient in EUV-induced ionospheric Hall conductance (Lotko et al., 2014). It becomes especially severe in simulations when conductance enhancements due to auroral precipitation are neglected (Smith, 2012), as in these simulations. Comparison of the 80F and 230F plasmasheets indicates that mass loading with O^+ fluid tends to counteract the effect, as evidenced by the greater mass loading and less asymmetric plasmasheet of 230F run. Brambles et al. (2010) showed that the plasmasheet is stretched tailward in MFLFM simulations when O^+ outflows are included. We may be seeing some manifestations of this effect in the asymmetric plasmasheets shown here, with average x-lines extending beyond $-60\ R_E$.

Noticeably more O^+ fluid is contained in the distant ($-30\ R_E$ to $-60\ R_E$), pre-midnight plasmasheet compared to the post-midnight plasmasheet, with the density asymmetry being especially prominent in the 80F run. Once the postmidnight plasmasheet contracts in tailward extent due to the aforementioned effect of ionospheric Hall conductance, access to the plasmasheet of the dawnside, tailward flowing lobe O^+ in the lobes is reduced, and more of the fluid exits the magnetosphere through the distant lobes without ever intersecting the postmidnight plasmasheet. This effect is less significant in the duskside lobes because the nightside x-line extends further tailward on the duskside. The duskward drift of the O^+ fluid in the lobes (Figure 6) also tends to transport

In Review

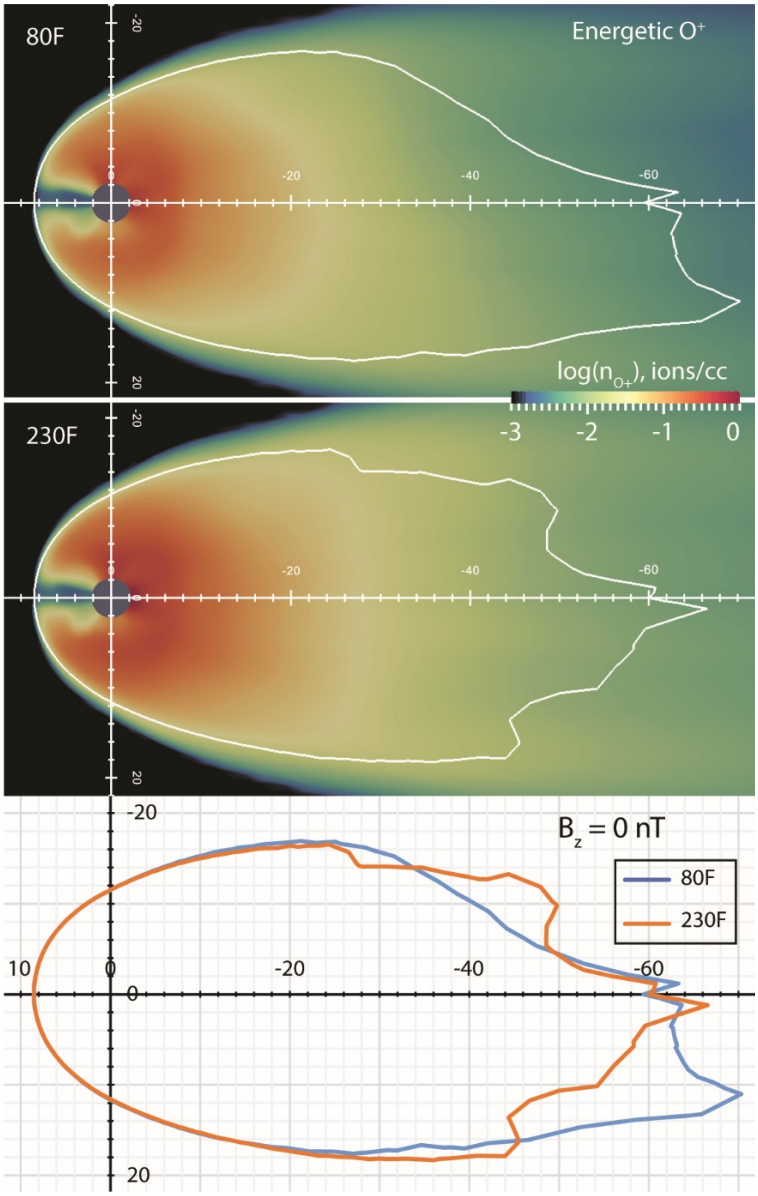


Figure 7. Log density of the energetic O^+ population (color scale) in the equatorial plane of the 80F (top) and 230F (middle) runs, time-averaged over the same 6-hour interval as in Fig. 2 and Table 1 (06-12 UT on 27 March). The white contours are average $B_z = 0$ contours corresponding to the average magnetic x-line. The dayside reconnection potential for each run is given in the lower left.

a portion of the the tailward flowing O^+, formerly in the dawnside lobe, toward the duskside by the time it intersects the plasmasheet. Transport of outflowing ionospheric O^+ into the plasmasheet from the ionosphere deserves a more comprehensive investigation than we have presented here. It involves many interacting processes that differ for dayside and nightside outflows.

Previous global simulations with O^+ outflows have shown that the CPCP decreases as the concentration of O^+ in the magnetosphere increases (Winglee et al., 2002; Brambles et al., 2010; Garcia et al., 2010; Wiltberger et al., 2010; Welling and Zaharia, 2012; Zhang et al., 2016b). We do not yet have a consensus on how exactly the addition of O^+ causes this change (Welling and Zaharia, 2012, and references therein). Ideal MHD does not allow field-aligned potential drops so the CPCP should scale linearly with the reconnection potential $\Delta\Phi_{Rx}$ along the dayside magnetopause. The integral of the simulated reconnection electric field E_{Rx} along the dayside x-line (between nulls in E_{Rx}) gives a dayside $\Delta\Phi_{Rx}$ of 181kV and 175kV for the 80F and 230F runs, respectively (Figure 8). When averaged over a long duration (e.g., the 6-hour interval used in Figures 3-7), the simulated nightside $\Delta\Phi_{Rx}$ should be approximately the negative of the dayside $\Delta\Phi_{Rx}$. Integration of E_{Rx} around the average $B_z = 0$ contour is, in fact, zero to within 0.1 kV in Figure 8. It is clear, however, that the average nightside reconnection rate inferred from the slope of the reconnection potential in Figure 8 is much larger than the dayside rate, which is distributed over a broader range of MLT.

The decrease in $\Delta\Phi_{Rx}$ for the 230F run is attributed to the greater density of O^+ in the reconnection inflow regions that feed magnetic diffusion along the magnetopause and the nightside x-line. Figure 7 (bottom) overlays the six-hour average $B_z = 0$ contours for the 80F and 230F runs for comparison. As measured by the $B_z = 0$ contours, the plasmasheet is smaller in size in the 230F run than 80F run, while the dayside magnetosphere from the subsolar point up to about $X = -20$ R_E is almost the same for the two runs. This comparison indicates that the dayside $\Delta\Phi_{Rx}$ is less in the 230F run primarily because E_{Rx} is less along the x-line in the 230F run relative to that in the 80F run. The reconnection rate scales with the Alfvén speed in the reconnection inflow region, and the reduction in the rate on the dayside in the 230F run is due largely to a reduction in Alfvén

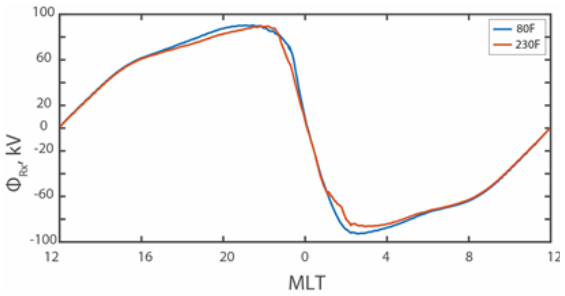


Figure 8. Average reconnection potential Φ_{Rx} vs MLT for the 80F and 230F runs. Φ_{Rx} is obtained by integrating the average reconnection electric field along the average x-line shown in Figure 7. Averages are computed for the six-hour simulation interval 06-12 March 27 2003.

speed, a consequence of the larger O^+ density (compare Figure 7 top and middle) and, therefore, in mass density in the inflow region earthward of the magnetopause.

Analysis of the nightside $\Delta\Phi_{Rx}$ is a bit more involved because both E_{Rx} and the length of the x-line change between the 80F and 230F runs. To evaluate the effect of mass loading on reconnection in these simulations, we consider the practically universal formula (Cassak et al., 2017) for the reconnection electric field $E_{Rx} = 0.1 v_{A,in} B_{in} = 0.1 B_{in}^2/\sqrt{\mu_0 \rho_{in}}$, where $v_{A,in}, B_{in}$ and ρ_{in} are the Alfvén speed, magnetic field and mass density in the reconnection inflow region (lobes for nightside reconnection). This relationship has also been verified in MFLFM simulations of outflow-induced, magnetotail sawtooth events at tail distances –20 R_E < X < –70 R_E wherein both B_{in} and ρ_{in} vary significantly over the course of a sawtooth cycle (Ouellette et al., 2013). We found that the simulated distribution of $0.1 B_x^2/\sqrt{\mu_0 \rho}$ in the Z = 1 R_E plane above the nightside x-line and within ± 1 hour of midnight in Figure 7 is about 10% less in the 230F run than the 80F run. This difference explains the lower reconnection potential for the 230F run in Figure 8.

The decrease in reconnection rate and Alfvén speed in the 230F run reduces its reconnection exhaust flows which stimulate down flowing Alfvénic Poynting fluxes in the plasmasheet (Zhang et al., 2012b). This feature is consistent with the reduction in $S_{||}$ on the nightside in the 230F run relative to the 80F run (Table 1). The connection between less intense $S_{||}$ and slower O^+ outflows is a feature of the phenomenological parameterization of wave-particle interactions in the IPWM model for transverse acceleration of O^+.

4. Conclusions

We isolated the nonelectrodynamic influence of the thermosphere on the coupled magnetosphere-ionosphere-thermosphere system by specifying a time-constant ionospheric conductance in the ionospheric Ohm's law used in global geospace simulations while allowing the thermosphere to modify the system state only through ionospheric ion outflows. The CMIT model coupled with the IPWM was used to study how the global system responds to different thermospheric states parameterized by F10.7, which regulates the solar EUV irradiance of the model thermosphere. Diagnostic comparisons were presented for F10.7 values of 80 and 230, representative of solar maximum and solar minimum thermospheres. The system was driven by solar wind/IMF conditions representative of an SIR that swept past Earth on 27 March 2003, but we used only the observed IMF Bz, solar wind density, V_x and sound speed as drivers to eliminate externally imposed asymmetries in the response caused by the neglected IMF and wind components.

Our principal results follow.

1. The cross polar cap potential is less when the thermosphere is exposed to higher solar EUV irradiance (F10.7 = 230) relative to a low irradiance state (F10.7 = 80). The effect is minor (4%) for the six-hour average states examined in the paper, but the instantaneous CPCP can exhibit differences up to 10% (Figure 2). The average reduction is attributed to a greater flux of O^+ outflow when the thermosphere is exposed to higher EUV irradiance.
2. The average outflow flux of transversely accelerated O^+ is 36% to 60% larger (dayside to nightside) for the 230F run relative to the 80F run (Table 1). This well-known dependence of the outflow flux on F10.7 must be due in large measure to the underlying thermospheric state. Average field-aligned outflow velocities are nearly the same on the dayside, but the average nightside outflow velocity decreases with increasing F10.7 (16% less for 230F run on the relative to the 80F run), as observed by the Akebono satellite. The decrease in nightside outflow velocity with increasing F10.7 in the simulations is a consequence of the higher outflow flux and greater mass loading of the plasmasheet at higher F10.7, which produces a lower nightside reconnection rate, slower reconnection exhaust flows, weaker earthbound

In Review

Alfvénic Poynting fluxes stimulated by the exhaust flows, and, therefore, less energy to power the transversely accelerated come field-aligned outflowing O^+.

3. The 80F and 230F runs both exhibit prenoon enhancements (relative to postnoon) in the O^+ outflow flux (Figure 3). The enhancement is most prominent in the 230F run, evidently very robust and commonly observed at altitudes ranging from the topside ionosphere into the low-altitude magnetosphere (~ 3 RE). We did not resolve the causal chain of events that produces it. Contributing factors include prenoon enhancements in i) Alfvénic Poynting flux (Figure 5), which determines the degree of transverse acceleration of O+ in the IPWM; ii) soft (~ 400 eV) electron precipitation (Figure 5), which contributes to enhanced ionosphere-thermosphere heating and, initially, an enhanced topside ambipolar electric field that raises the scale height of the O^+ source region; and iii) modest increase in scale height of atomic O (SI Figure S3), which also contributes to enhanced O^+ production. Solar illumination-induced thermal expansion of the ionosphere may also contribute as proposed by Redmon et al. (2012).
4. The simulations exhibit relatively large nightside Alfvénic Poynting fluxes (Figure 5) that do not produce O^+ outflows as profuse as those emerging from the dayside ionosphere-thermosphere. Since the average topside O^+ density on the nightside is comparatively lower (as inferred from $F_{O^+}/\bar{V}_{\|O^+}$ in Table 1), for the same amplitude of Alfvénic power available for transverse acceleration, the outflow flux should be comparatively lower on the nightside.
5. The dawnside enhancement in O^+ outflow flux observed by Cluster in the lobes is a direct consequence in the simulations of the prenoon enhancement in outflow flux at low altitudes. The lobe outflow experiences a duskward $\boldsymbol{E}\times\boldsymbol{B}$ drift (Figure 6), which is attributed to the asymmetry in ionospheric convection resulting from the sunward gradient in the Hall conductance. All simulations were performed with the same EUV-induced ionospheric conductance.
6. The O^+ density of the 230F-simulated plasmasheet is greater on average than that of the 80F plasmasheet (Figure 7). This dependence on F10.7 was first reported in early ISEE satellite measurements and more recently in Cluster satellite measurements. The magnitude of the plasmasheet O^+ density is comparable to observed values in the midtail region ($-X_{SM}$ from 15-20 R_E). Pre/post-midnight asymmetry in the plasmasheet O^+ density is relatively weak in the midtail region (observationally and as simulated), but it becomes significant in the simulations at greater radial distances (Figure 7).
7. The 230F plasmasheet is smaller in extent than the 80F plasmasheet as measured by the area enclosed by the nightside x-line, and it is more symmetric across midnight than the 80F plasmasheet (Figure 7). The severe contraction of the post-midnight plasmasheet relative to pre-midnight attributed to the sunward gradient in ionospheric Hall conductance is almost entirely counteracted in the simulations by O^+ mass loading of the 230F plasmasheet. Access to the postmidnight plasmasheet by lobe O^+ is consequently greater in the 230F run because the postmidnight x-line extends further tailward in the 230F run than in the 80F run.
8. The reconnection rate is less for the 230F case than for the 80F case because the greater flux of ionospheric O^+ into the lobes and dayside magnetosphere mass loads the inflow region for reconnection and yields a lower inflow rate of magnetic flux $\left(0.1 v_{A,in}\, B_{in}\right)$ to feed reconnection. The outcome at higher F10.7 is lower dayside and nightside reconnection potentials (Figure 8) and cross polar cap potential (Figure 2).

We emphasize that the only difference in inputs to the 230F and 80F simulations is the thermospheric state parameterized by F10.7. All other input parameters and driving of the simulations are otherwise identical. Thus the simulated differences in states of the ionosphere including its distributions of O^+ outflow into the magnetosphere and polar cap potential, O^+ fluxes in the magnetotail lobes, and O^+ loading of the plasmasheet and nightside reconnection can all be attributed to the different initial states of the thermosphere. With the same time-constant conductance in both simulations, the only pathway for the thermosphere to influence the geospace system is through its influence on ionospheric outflows, directly via topside O^+ production and upwelling and indirectly via induced changes in the magnetosphere-ionosphere-thermosphere interaction.

The differences summarized above are qualitatively consistent with a variety of observations, but they are not likely to be quantitatively consistent. In order to isolate the nonelectrodynamic influence of the thermosphere on the geospace system, we contrived to exclude other important effects. Foremost among these are dynamic

variations in ionospheric conductance that feedback into magnetospheric dynamics via convection and closure of field-aligned currents. We have demonstrated for the first time that the thermosphere can influence the magnetosphere through ionospheric ion outflows using a self-consistent coupled MIT model that includes ionospheric outflows.

Acknowledgments

IMF and Solar wind data were provided by J.H. King, N. Papatashvilli at AdnetSystems, NASA GSFC and CDAWeb. We acknowledge support by the National Center for Atmospheric Research, a major facility sponsored by the National Science Foundation under Cooperative Agreement No. 1852977, NSF awards 1739188, 1522133 and the Thayer School of Engineering at Dartmouth College. Computing resources were provided by NCAR's Computational and Information Systems Laboratory (CISL). WL and RV were additionally supported by NASA grant 80NSSC19K0071. Model results used to produce the plots shown are available at https://doi.org/10.5065/77g1-9x56 .

References

Abe, T., Yau, A. W., Watanabe, S., Yamada, M., and Sagawa, E. (2004), Long-term variation of the polar wind velocity and its implication for the ion acceleration process: Akebono/suprathermal ion mass spectrometer observations, J. Geophys. Res., 109, A09305, doi:10.1029/2003JA010223.

Andersson, L., W. K. Peterson, and K. M. McBryde (2005), Estimates of the suprathermal O+ outflow characteristic energy and relative location in the auroral oval, Geophys. Res. Lett., 32, L09104, doi:10.1029/2004GL021434.

Blanc, M., and Richmond, A. (1980), The ionospheric disturbance dynamo, J. Geophys. Res., 85(A4), 1669–1686, doi:10.1029/JA085iA04p01669.

Bouhram, M., B. Klecker, W. Miyake, H. Reme, J. A. Sauvaud, M. Malingre, L. Kistler, and A. Blagau (2004), On the altitude dependence of transversely heated O+ distributions in the clusp/cleft, Ann. Geophys., 22, 1787–1798.

Brambles, O. J., W. Lotko, P. A. Damiano, B. Zhang, M. Wiltberger, and J. Lyon (2010), Effects of causally driven cusp O+ outflow on the storm time magnetosphere-ionosphere system using a multifluid global simulation, J. Geophys. Res., 115, A00J04, doi:10.1029/2010JA015469.

Brambles, O. J., W. Lotko, B. Zhang, M. Wiltberger, J. Lyon, and R. J. Strangeway (2011), Magnetosphere sawtooth oscillations induced by ionospheric outflow, Science, 332(6034), 1183–1186, doi:10.1126/science.1202869.

Brekke, A., and J. Moen, Observations of high latitude ionospheric conductances, J. Atmos. Terr. Phys., 55, 1493–1512, 1993.

Cannata, R. W., and T. I. Gombosi (1989), Modeling the solar cycle dependence of quiet-time ion upwelling at high geomagnetic latitudes, Geophys. Res. Lett., 16, 1141–1144.

Carlson, H. C., Spain, T., Aruliah, A., Skjaeveland, A., and Moen, J. (2012), First-principles physics of cusp/polar cap thermospheric disturbances, Geophys. Res. Lett., 39, L19103, doi:10.1029/2012GL053034.

Cassak, P. A., Liu, Y.-H. & Shay, M. A. (2017), A review of the 0.1 reconnection rate problem. Journal of Plasma Physics 83, 1-17. doi:10.1017/S0022377817000666.

Connor, H. K., Zesta, E., Ober, D. M., and Raeder, J. (2014), The relation between transpolar potential and reconnection rates during sudden enhancement of solar wind dynamic pressure: OpenGGCM-CTIM results, J. Geophys. Res. Space Physics, 119, 3411– 3429, doi:10.1002/2013JA019728.

Evans, J. V. (1975), A study of F2 region daytime vertical ionization fluxes at Millstone Hill during 1969, Planet. Space Sci., 23, 1461–1482, doi:10.1016/0032-0633(75)90001-X.

Fang, X., Randall, C. E., Lummerzheim, D., Solomon, S. C., Mills, M. J., Marsh, D. R., Jackman, C. H., Wang, W., and Lu, G. (2008), Electron impact ionization: A new parameterization for 100 eV to 1 MeV electrons, J. Geophys. Res., 113, A09311, doi:10.1029/2008JA013384.

Fedder, J. A., and J. G. Lyon (1987), The solar wind-magnetosphere-ionosphere current-voltage relationship, Geophys. Res. Lett., 14(8), 880–883, doi:10.1029/GL014i008p00880.

Foster, J. C., and Vo, H. B. (2002), Average characteristics and activity dependence of the subauroral polarization stream, J. Geophys. Res., 107(A12), 1475, doi:10.1029/2002JA009409.

Garcia, K. S., V. G. Merkin, and W. J. Hughes (2010), Effects of nightside O + outflow on magnetospheric

dynamics: Results of multifluid MHD modeling, J. Geophys. Res., 115, A00J09, doi:10.1029/2010JA015730.

Garcia-Sage, K., Moore, T. E., Pembroke, A., Merkin, V. G., and Hughes, W. J. (2015), Modeling the effects of ionospheric oxygen outflow on bursty magnetotail flows, J. Geophys. Res. Space Physics, 120, 8723–8737, doi:10.1002/2015JA021228.

Giles, B. L., C. R. Chappell, T. E. Moore, R. H. Comfort, and J. H. Waite Jr. (1994), Statistical survey of pitch angle distributions in core (0–50 eV) ions from Dynamics Explorer: 1. Outflow in the auroral zone, polar cap, and cusp, J. Geophys. Res., 99, 17,483–17,501, doi:10.1029/ 94JA00864.

Glocer, A., G. Tóth, T. Gombosi, and D. Welling (2009), Modeling ionospheric outflows and their impact on the magnetosphere, initial results, J. Geophys. Res., 114, A05216, doi:10.1029/2009JA014053.

Glocer A., Toth, G., & Fok, M.-C. (2018). Including kinetic ion effects in the coupled global ionospheric outflow solution. Journal of Geophysical Research: Space Physics, 123, 2851–2871. https://doi.org/10.1002/2018JA025241.

Hedin, A. E., and Mayr, H. G. (1987), Solar EUV induced variations in the thermosphere, J. Geophys. Res., 92(D1), 869– 875, doi:10.1029/JD092iD01p00869.

Hines, CO . (1974), The Upper Atmosphere in Motion, Geophys. Monogr. Ser., vol. 18, AGU , Washington , D.C..

Jian, L., Russel, C. T., Luhmann, J. G., Skoug, R. M. (2006). Properties of Stream Interactions at One AU During 1995 – 2004. Solar Physics, 239(1-2), 337–392. https://doi.org/10.1007/s11207-006-0132-3.

Kistler, L. M., et al. (2005), Contribution of nonadiabatic ions to the cross-tail current in an O+ dominated thin current sheet, J. Geophys. Res., 110, A06213, doi:10.1029/2004JA010653.

Lennartsson, W. (1989), Energetic (0.1- to 16-keV/e) magnetospheric ion composition at different levels of solar F10.7, J. Geophys. Res., 94(A4), 3600– 3610, doi:10.1029/JA094iA04p03600.

Lennartsson, O. W., Collin, H. L., and Peterson, W. K. (2004), Solar wind control of Earth's H+ and O+ outflow rates in the 15-eV to 33-keV energy range, J. Geophys. Res., 109, A12212, doi:10.1029/2004JA010690.

Liao, J., Kistler, L. M., Mouikis, C. G., Klecker, B., Dandouras, I., and Zhang, J.-C. (2010), Statistical study of O+ transport from the cusp to the lobes with Cluster CODIF data, J. Geophys. Res., 115, A00J15, doi:10.1029/2010JA015613.

Liao, J., Kistler, L. M., Mouikis, C. G., Klecker, B., and Dandouras, I. (2012), Solar cycle dependence of the cusp O+access to the near-Earth magnetotail, J. Geophys. Res., 117, A10220, doi:10.1029/2012JA017819.

Liu, J., Wang, W., Zhang, B., Huang, C., & Lin, D. (2018). Temporal variation of solar wind in controlling solar wind-magnetosphere-ionosphere energy budget. Journal of Geophysical Research: Space Physics, 123, 5862– 5869. https://doi.org/10.1029/2017JA025154.

Lockwood, M., J. H. Waite Jr., T. E. Moore, J. F. E. Johnson, and C. R. Chappell (1985), A new source of O+ ions near the dayside polar cap boundary, J. Geophys. Res., 90,4099–4116, doi:10.1029/JA090iA05p04099.

Lotko, W. (2007). The magnetosphere-ionosphere system from the perspective of plasma circulation: A tutorial, J. Atmos. Sol. Terr. Phys., 69, 191–211, doi:10.1016/j.jastp.2006.08.011.

Lotko, W., R. H. Smith, B. Zhang, J. E. Ouellette, O. J. Brambles, and J. G. Lyon (2014), Ionospheric control of magnetotail reconnection, Science, 345(6193), 184–187, doi:10.1126/science.1252907.

Lyon, J., J. Fedder, and C. Mobarry (2004), The Lyon-Fedder-Mobarry (LFM) global MHD magnetospheric simulation code, J. Atmos. Sol. Terr. Phys., 66(15–16), 1333–1350, doi:10.1016/j.jastp.2004.03.020.

Maggiolo, R., and Kistler, L. M. (2014), Spatial variation in the plasma sheet composition: Dependence on geomagnetic and solar activity, J. Geophys. Res. Space Physics, 119, 2836– 2857, doi:10.1002/2013JA019517.

Merkin, V. G., and J. G. Lyon (2010), Effects of the low-latitude ionospheric boundary condition on the global magnetosphere, J. Geophys. Res., 115, A10202, doi:10.1029/2010JA015461.

Merkin, V. G., Panov, E. V., Sorathia, K., & Ukhorskiy, A. Y. (2019). Contribution of bursty bulk flows to the global dipolarization of the magnetotail during an isolated substorm. Journal of Geophysical Research: Space Physics, 124, 8647– 8668, doi:10.1029/2019JA026872 .

Mouikis, C. G., Kistler, L. M., Liu, Y. H., Klecker, B., Korth, A., and Dandouras, I. (2010), H+ and O+ content of the plasma sheet at 15–19 Re as a function of geomagnetic and solar activity, J. Geophys. Res., 115, A00J16, doi:10.1029/2010JA015978.

Nakamura, R., et al. (2004), Spatial scale of high-speed flows in the plasma sheet observed by Cluster, Geophys. Res. Lett., 31, L09804, doi:10.1029/2004GL019558.

In Review

Nosé, M., R. W. McEntire, and S. P. Christon (2003), Change of the plasma sheet ion composition during magnetic storm development observed by the Geotail spacecraft, J. Geophys. Res., 108(A5), 1201, doi:10.1029/2002JA009660.

Ohtani, S., Wing, S., Merkin, V. G., and Higuchi, T. (2014), Solar cycle dependence of nightside field-aligned currents: Effects of dayside ionospheric conductivity on the solar wind-magnetosphere-ionosphere coupling, J. Geophys. Res. Space Physics, 119, 322– 334, doi:10.1002/2013JA019410.

Ouellette, J. E., Rogers, B. N., Wiltberger, M., and Lyon, J. G. (2010), Magnetic reconnection at the dayside magnetopause in global Lyon-Fedder-Mobarry simulations, J. Geophys. Res., 115, A08222, doi:10.1029/2009JA014886.

Ouellette, J. E., Brambles, O. J., Lyon, J. G., Lotko, W., and Rogers, B. N. (2013), Properties of outflow-driven sawtooth substorms, J. Geophys. Res. Space Physics, 118, 3223– 3232, doi:10.1002/jgra.50309.

Pham, K. H. (2020). LIT Thermosphere Control of Ion Outflow Results, UCAR/NCAR - DASH Repository. https://doi.org/10.5065/77g1-9x56 .

Picone, J. M., Hedin, A. E., Drob, D. P., and Aikin, A. C. (2002). NRLMSISE-00 empirical model of the atmosphere: Statistical comparisons and scientific issues, J. Geophys. Res., 107(A12), 1468, doi:10.1029/2002JA009430.

Pollock, C. J., M. O. Chandler, T. E. Moore, J. H. Waite Jr., C. R. Chappell, and D. A. Gurnett (1990), A survey of upwelling ion event characteristics, J. Geophys. Res., 95, 18,969–18,980, doi:10.1029/JA095iA11p18969.

Qian, L., Burns, A.G., Emery, B.A., Foster, B., Lu, G., Maute, A., Richmond, A.D., Roble, R.G., Solomon, S.C. and Wang, W. (2014). The NCAR TIE-GCM: A Community Model of the Coupled Thermosphere/Ionosphere System. In Modeling the Ionosphere–Thermosphere System (eds J. Huba, R. Schunk and G. Khazanov). doi:10.1002/9781118704417.ch7

Raeder, J. (2003). Global Geospace Modeling: Tutorial and Review, in Space Plasma Simulation, edited by: J. B¨uchner, C. T. Dum, and M. Scholer, Lecture Notes in Physics 615, Springer Verlag, Berlin, 2003. ISBN 3-540-00698-2.

Raeder, J., W. D. Cramer, J. Jensen, T. Fuller-Rowell, N. Maruyama, F. Toffoletto, and H. Vo (2016), Sub-auroral polarization streams: A complex interaction between the magnetosphere, ionosphere, and thermosphere, J. Phys. Conf. Ser., 767(1), 012021, doi:10.1088/1742-6596/767/1/012021.

Redmon, R. J., Peterson, W. K., Andersson, L., and Richards, P. G. (2012), Dawnward shift of the dayside O+ outflow distribution: The importance of field line history in O+ escape from the ionosphere, J. Geophys. Res., 117, A12222, doi:10.1029/2012JA018145.

Richards, P. G. (2011), Reexamination of ionospheric photochemistry, J. Geophys. Res., 116, A08307, doi:10.1029/2011JA016613.

Ridley, A. J., T. I. Gombosi, and D. L. De Zeeuw (2004), Ionospheric control of the magnetospheric configuration: Conductance, Ann. Geophys., 22, 567.

Roble, R. G. and E. C. Ridley (1987), An auroral model for the NCAR thermosphere general circulation model (TGCM, Annales. Geophysicae, 5A, 6, 369–382.

Senior, C., and Blanc, M. (1984), On the control of magnetospheric convection by the spatial distribution of ionospheric conductivities, J. Geophys. Res., 89(A1), 261– 284, doi:10.1029/JA089iA01p00261.

Smith, R. (2012). Effects of ionospheric conductance on magnetosphere-ionosphere coupling, (MS thesis). Hanover, NH: Thayer School of Engineering, Dartmouth College, https://search.proquest.com/docview/1318498884?pq-origsite=summon.

Solomon, S. C., and L. Qian (2005), Solar extreme-ultraviolet irradiance for general circulation models, J. Geophys. Res., 110, A10306, doi:10.1029/2005JA011160.

Thayer, J. P., and J. Semeter (2004), The convergence of magnetospheric energy flux in the polar atmosphere, J. Atmos. Sol. Terr. Phys., 66, 807–824, doi:10.1016/j.jastp.2004.01.035.

Varney, R. H., Solomon, S. C., and Nicolls, M. J. (2014), Heating of the sunlit polar cap ionosphere by reflected photoelectrons, J. Geophys. Res. Space Physics, 119, 8660– 8684, doi:10.1002/2013JA019378.

Varney, R. H., M. Wiltberger, and W. Lotko (2015), Modeling the interaction between convection and nonthermal ion outflows, J. Geophys. Res. Space Physics, 120, 2353–2362, doi:10.1002/2014JA020769.

Varney, R. H., M. Wiltberger, B. Zhang, W. Lotko, and J. Lyon (2016a), Influence of ion outflow in coupled geospace simulations: 1. Physics-based ion outflow model development and sen- sitivity study, J. Geophys. Res. Space Physics, 121, 9671–9687, doi:10.1002/2016JA022777.

In Review

Varney, R., M. Wiltberger, B. Zhang, W. Lotko, and J. Lyon (2016b), Influence of ion outflow in coupled geospace simulations: 2. Sawtooth oscillations driven by physics-based ion outflow, J. Geophys. Res. Space Physics, 121, 9688–9700, doi:10.1002/2016JA022778.

Wang, W., M. Wiltberger, A. G. Burns, S. C. Solomon, T. L. Killeen, N. Maruyama, and J. G. Lyon (2004), Initial results from the coupled magnetosphere-ionosphere-thermosphere model: Thermosphere-ionosphere responses, J. Atmos. Sol. Terr. Phys., 66(15–16), 1425–1441, doi:10.1016/j.jastp.2004.04.008.

Wang, W., Lei, J., Burns, A. G., Wiltberger, M., Richmond, A. D., Solomon, S. C., Killeen, T. L., Talaat, E. R., and Anderson, D. N. (2008), Ionospheric electric field variations during a geomagnetic storm simulated by a coupled magnetosphere ionosphere thermosphere (CMIT) model, Geophys. Res. Lett., 35, L18105, doi:10.1029/2008GL035155.

Weiss, L.A., P.H. Reiff, J.J. Moses, R.A. Heelis, and D.B. Moore (1992), Energy dissipation in substorms. Substorms I, ESA SP-335, Paris, Eur. Space Agency, 309–317.

Welling, D. T., and Zaharia, S. G. (2012), Ionospheric outflow and cross polar cap potential: What is the role of magnetospheric inflation?, Geophys. Res. Lett., 39, L23101, doi:10.1029/2012GL054228.

Wiltberger, M., W. Wang, A. G. Burns, S. Solomon, J. Lyon, and C. Goodrich (2004), Initial results from the coupled magnetosphere ionosphere thermosphere model: Magnetospheric and ionospheric responses, J. Atmos. Sol. Terr. Phys., 66(15–16), 1411–1423, doi:10.1016/j.jastp.2004.03.026.

Wiltberger, M., Weigel, R. S., Lotko, W., and Fedder, J. A. (2009), Modeling seasonal variations of auroral particle precipitation in a global-scale magnetosphere-ionosphere simulation, J. Geophys. Res., 114, A01204, doi:10.1029/2008JA013108.

Wiltberger, M., W. Lotko, J. G. Lyon, P. Damiano, and V. Merkin (2010), Influence of cusp O + outflow on magnetotail dynamics in a multifluid MHD model of the magnetosphere, J. Geophys. Res., 115, A00J05, doi:10.1029/2010JA015579.

Wiltberger, M., L. Qian, C.-L. Huang, W. Wang, R. E. Lopez, A. G. Burns, S. C. Solomon, Y. Deng, and Y. Huang (2012), CMIT study of CR2060 and 2068 comparing L1 and MAS solar wind drivers, J. Atmos. Sol. Terr. Phys., 83, 39–50, doi:10.1016/j.jastp.2012.01.005.

Wiltberger, M., Merkin, V., Lyon, J. G., and Ohtani, S. (2015), High-resolution global magnetohydrodynamic simulation of bursty bulk flows. J. Geophys. Res. Space Physics, 120, 4555– 4566. doi: 10.1002/2015JA021080.

Winglee, R. M., D. Chua, M. Brittnacher, G. K. Parks, and G. Lu (2002), Global impact of ionospheric outflows on the dynamics of the magnetosphere and cross-polar cap potential, J. Geophys. Res., 107(A9), 1237, doi:10.1029/2001JA000214.

Yau, A. W., W. K. Peterson, and T. Abe (2011), Influences of the ionosphere, thermosphere and magnetosphere on ion outflows, in The Dynamic Magnetosphere, IAGA Special Sopron Book Ser., vol. 3, edited by A. W. Yau, W. K. Peterson, and T. Abe, pp. 283–314, Springer, Dordrecht, Netherlands, doi:10.1007/978-94-007-0501-2_16.

Yau, A.W., Peterson, W.K. and Shelley, E.G. (2013). Quantitative Parametrization of Energetic Ionospheric Ion Outflow. In Modeling Magnetospheric Plasma (eds T.E. Moore, J.H. Waite, T.W. Moorehead and W.B. Hanson). doi:10.1029/GM044p0211.

Zhang, B., Lotko, W., Brambles, O., Wiltberger, M., Wang, W., Schmitt, P., and Lyon, J. (2012a), Enhancement of thermospheric mass density by soft electron precipitation, Geophys. Res. Lett., 39, L20102, doi:10.1029/2012GL053519.

Zhang, B., Lotko, W., Brambles, O., Damiano, P., Wiltberger, M., and Lyon, J. (2012b), Magnetotail origins of auroral Alfvénic power, J. Geophys. Res., 117, A09205, doi:10.1029/2012JA017680.

Zhang, B., Varney, R. H., Lotko, W., Brambles, O. J., Wang, W., Lei, J., Wiltberger, M., and Lyon, J. G. (2015a), Pathways of F region thermospheric mass density enhancement via soft electron precipitation, J. Geophys. Res. Space Physics, 120, 5824– 5831, doi:10.1002/2015JA020999.

Zhang, B., Lotko, W., Brambles, O., Wiltberger, M. and Lyon, J. (2015b), Electron precipitation models in global magnetosphere simulations. J. Geophys. Res. Space Physics, 120: 1035– 1056. doi:10.1002/2014JA020615.

Zhang, B., O. J. Brambles,W. Lotko, J. E. Ouellette, and J. G. Lyon (2016a), The role of ionospheric O+ outflow in the generation of earthward propagating plasmoids, J. Geophys. Res. Space Physics, 121, 1425–1435, doi:10.1002/2015JA021667.

Zhang, B., Brambles, O. J., Wiltberger, M., Lotko, W., Ouellette, J. E., and Lyon, J. G. (2016b), How does mass loading impact local versus global control on dayside reconnection? Geophys. Res. Lett., 43, 1837–1844, doi:10.1002/2016GL068005.

In review

In Review

SUPPORTING INFORMATION

Thermospheric Impact on the Magnetosphere through Ionospheric Outflow

K. H. Pham[1], W. Lotko[1,2], R. H. Varney[3], B. Zhang[4], and J. Liu[5]

[1] High Altitude Observatory, National Center for Atmospheric Research, Boulder, CO, USA.
[2] Thayer School of Engineering, Dartmouth College, Hanover, NH USA.
[3] Center for Geospace Studies, SRI International, Menlo Park, CA, USA.
[4] Department of Earth Sciences, University of Hong Kong, Pokfulam, Hong Kong.
[5] Institute of Space Sciences, Shandong University, Weihai, China.

In Review

Contents of Supporting Information

Text S1 to S3
Figures S1 to S3

Introduction

This Supporting Information includes the following sections and figures:

Text S1. Description of Models

Text S2. LIT Coupling Scheme and Figure S1 a schematic of the coupling scheme.

Text S3. Neutral profile at the pre and post noon points of interest.

Figure S2. The solar wind parameters used to drive the simulation runs.

Figure S3. Neutral density and temperature altitude profiles for the two points of interests marked as magenta crosses on Figure 3.

Text S1. Description of Models

The multifluid extension of the Lyon-Fedder-Mobarry (LFM) expands upon the single-fluid ideal MHD equations by giving each fluid species distinct equations for mass continuity, momentum, and energy. A feature of the approach is that the velocity perpendicular to the magnetic field coincides with the electrical drift velocity, which results in the same perpendicular velocity for all ion species. However, the parallel motion of the individual species can evolve independently, though with constraints imposed by collective effects on the magnetic field evolution. The fluids can correspond to any species without limitation, including multiple fluids of the same species. Here, we follow the fluid convention established by the Varney et al. (2016a) with simulation of two H^+ fluids (one for H^+ of solar wind origin, and another for polar wind H^+) and two O^+ fluids (one for polar wind O^+ and one for transversely accelerated energetic O^+). The MFLFM grid is a distorted sphere with axis of symmetry along the x_{sm} axis (SM indicates Solar Magnetic coordinate system). It extends from 30 R_E upstream of Earth to 300 R_E downstream and 100 R_E radially on the sides. For this study, MFLFM is used in what is referred to in the LFM literatures as a double-resolution (53x48x64 in the radial, azimuthal, and meridional) configuration. A more detailed description of the underlying LFM can be found in Lyon et al. (2004) and a description of the multifluid extension of the MHD equations can be found in Wiltberger et al. (2010).

The magnetosphere-ionosphere exchange (MIX) acts as the interface that transforms quantities derived from one model into quantities that are used in the other models. It takes field-aligned currents from LFM and the ionospheric conductance (Σ) derived from TIEGCM to solve a boundary value problem for the electrostatic potential (Φ). One unique capability of MIX is its specification of three distinct electron precipitation populations: monoenergetic and diffuse precipitation (monodiffuse), broadband electron precipitation (BBE), and direct-entry cusp electron precipitation (cusp) (Zhang et al., 2015). The precipitating number flux and mean energy of each type of precipitation are derived from MHD parameters provided by LFM and they evolve dynamically as a result of changes in the magnetosphere. Each electron precipitation type have different and wide ranging influence on the thermosphere-ionosphere system (e.g. Zhang et al., 2012a). For the double-resolution LFM, MIX has a grid resolution of approximately 2° in both longitude and latitude in SM coordinates (MLON and MLAT, respectively), approximately matching the LFM inner boundary magnetically mapped down to an altitude of 100 km in the ionosphere. The MIX low-latitude boundary is located at 46° MLAT, which corresponds to a dipole field line that maps to $2R_E$ at the equator. A more detailed description of the MIX Poisson solver can be found in Merkin & Lyon (2010).

TIEGCM solves fluid equations for the neutral gas species on a global geographic grid with a resolution of 1.25° for both latitude and longitude. The TIEGCM height profile is resolved at constant pressure levels. The lowest pressure level also corresponds to the TIEGCM low altitude boundary, which is fixed at 97 km, while the high-altitude boundary varies with solar cycle, usually ranging from 400km at solar min to 800km at solar max. As the Thermosphere-Ionosphere Electrodynamic General Circulation Model, TIEGCM models the global thermosphere and ionosphere system by solving the three-dimensional, fully coupled, hydrodynamic, thermodynamic, and continuity equations of neutral gases self-consistently while the ions are modeled using a finite differencing scheme (Roble et al., 1988). A more detailed description of TIEGCM can be found in Wang et al. (2004) and Qian et al., (2014).

In Review

IPWM is a 3D ion transport model of the high-latitude ionosphere that solves the eight-moment equations for the parallel transport of H^+, He^+, O^+ (^4S), and electrons and also includes the photochemistry of N^+, NO^+, $N2^+$ O_2^+, O^+ (^2D) and O^+ (^2P). As input, IPWM requires neutral thermospheric information from an external source, either NRLMSISE-00 or TIEGCM but mostly comes from TIEGCM in our coupled model. IPWM also includes an extra fluid to model nonthermal O^+ that obeys a different set of transport equations. The nonthermal O^+ are thermal O^+ that have been transversely accelerated via a phenomenological wave-particle interaction model. Further details of the method can be found in Varney et al. (2015). We refer to nonthermal O^+ and energetic O^+ interchangeably. The IPWM grid uses a nonorthogonal grid that is defined such that at low altitudes (~100km), the longitude and latitude is approximately 2° separation and follows the field-aligned upwards. Due to the nonorthogonality of the grid, the longitudinal and latitudinal size of the grid also expands with the field lines when they spread at higher altitudes. The IPWM altitude ranges from the same TIEGCM lower altitude boundary of 97km up to 8400km, where the lower latitude at 97km approximately maps along field lines to 4 R_E at the equator, and to 2.2 R_E. We define outflow into the magnetosphere as any upward flux at 1R_E altitude. A more detailed description of the IPWM grid can be found in the supporting documents in Varney et al. (2015).

Text S2. LIT Coupling Scheme

The LIT coupling scheme is shown in Figure S1. For simplicity, the overview starts from LFM to MIX coupling; however, while running, the communications between the components are performed simultaneously with an exchange time of every 5 seconds. MIX obtains the MHD density (ρ), temperature (or sound speed, c_s), and field-aligned currents ($J_{||}$) at the LFM low-altitude boundary. It also receives a 180s running average downward field-aligned Poynting flux ($S_{||}$) from LFM, derived from its fields obtained four cells above the low-altitude boundary and mapped along dipole field lines to 100 km altitude. This Poynting flux is representative of downward flowing Alfvén wave power and is used in MIX's empirical model for the flux and mean energy of BBE precipitation. The MHD ρ, c_s, and $J_{||}$ are used by MIX to empirically estimate the number flux (F) and mean energy (E) of three distinct electron precipitation populations: the monoenergetic and diffuse electron precipitations and the direct-entry cusp electrons (cusp) (Zhang et al., 2015). MIX uses the field-aligned currents that it receives from LFM in conjunction with the ionospheric conductance (Σ), that it receives from TIEGCM, to solve a boundary value problem for the electrostatic potential (Φ). Once calculated, MIX passes Φ to all three models, LFM, TIEGCM, and IPWM, while F and E of all the derived electron populations are passed to TIEGCM and IPWM.

TIEGCM then deposits the precipitating energy flux of each electron population at altitudes specified by Fang et al. (2008). The harder (more energetic) electron precipitation, namely the monodiffuse, is typically deposited in the E region while the softer (100-1000eV) electron precipitation, BBE and cusp populations, typically deposit energy in the F region (Zhang et al., 2012a). The convection pattern associated with Φ contributes to Joule heating. The evolving ionospheric conductance derived from TIEGCM is then passed back to MIX. We consider the above coupling as the electrodynamic coupling pathway. Details of this coupling is described further in Wiltberger et al. (2004) and Wang et al. (2008).

In Review

IPWM uses the MIX quantities in a similar manner as TIEGCM based on the Fang et al. (2008) method. Additionally, $S_{||}$ is also passed from LFM through MIX to get to IPWM. $S_{||}$ is used to regulate the altitude and rate of transverse ion acceleration. This acceleration starts at higher altitude and at a lower rate for lower values of $S_{||}$. Detailed description of the IPWM transverse ion acceleration method can be found in Varney et al. (2015) and Varney et al. (2016a). The densities, velocities, and sound speeds of any outflowing species are passed to MFLFM, where they are treated as separate fluids. MFLFM evolves 4 different fluids: solar wind H^+, outflow of H^+, outflow of thermal O^+, and outflow of energetic O^+ (Varney et al., 2016a). A detailed discussion of the coupling of IPWM to the MFLFM at LFM's low-altitude boundary can be found in Varney et al. (2016a).

IPWM does not simulate the thermosphere and requires the thermosphere to be externally provided, using both TIEGCM and the empirical thermosphere model NRLMSISE-00 (Picone et al., 2002). The thermosphere provides the neutral density (N_n), neutral temperature (T_n), and the neutral wind (u_n) at all latitudes, longitudes, and altitudes to IPWM. As opposed to NRLMSISE-00, TIEGCM is capable of also providing neutral wind information and, more importantly, provides them in a self-consistent way; however, TIEGCM does not provide H or He information, and therefore, IPWM must continue to receive the H and He profiles from NRLMSISE-00, while all other neutral species can be obtained by TIEGCM. The addition of neutral wind information is important for better estimation of ion-neutral frictional heating (Carlson et al., 2012; Thayer and Semeter, 2004) in IPWM. All thermospheric information is then interpolated and extrapolated onto IPWM's grid. The IPWM altitude grid extends from approximately TIEGCM's lower altitude boundary of 97km all the way up to approximately 8400 km, which lies well above TIEGCM's upper altitude boundary. To handle the neutral parameters above TIEGCM's grid, we assume hydrostatic equilibrium and extrapolate upwards.

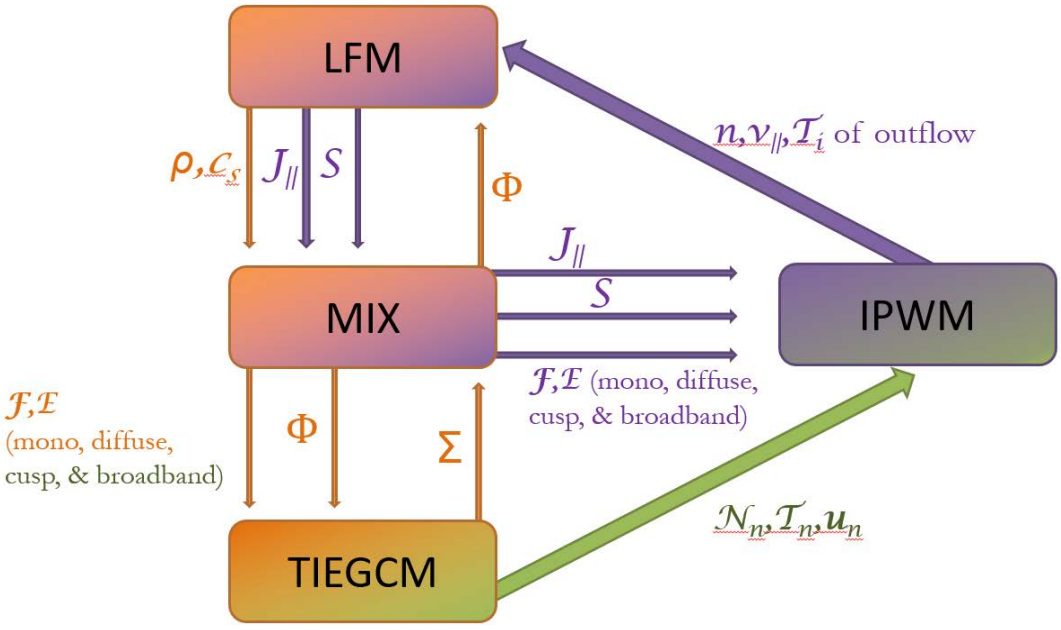


Figure S1. Schematic of the coupling between the models. Orange boxes and arrows are for CMIT coupling, purple for MFLFM-IPWM coupling, and everything, including the green, is the LIT coupling.

Text S3. LIT Preconditioning

The goal of the spin-up procedure is to reduce the influence and memory of each model's initial state. For LFM-MIX, the procedure is to start from an empty dipole and then to simulate 50 minutes of no IMF, followed by 2 hours of southward B_z then by 2 hours of northward IMF. This first removes any numerical artifacts due to the empty dipole start and then loads the magnetosphere with plasma through magnetic reconnection.

TIEGCM's initial state is derived from an average thermosphere-ionosphere state that is representative of a solar maximum equinox. TIEGCM is then driven in the high latitude by the LFM-MIX's last initialization state (end of 2 hour northward IMF period) for 5 days. This should be a sufficient amount of time to align the TIEGCM solution with LFM-MIX's.

The final initialization state from TIEGCM and LFM-MIX are used to spin up IPWM for 12 hours. After each model's initialization, all models are coupled together going forward.

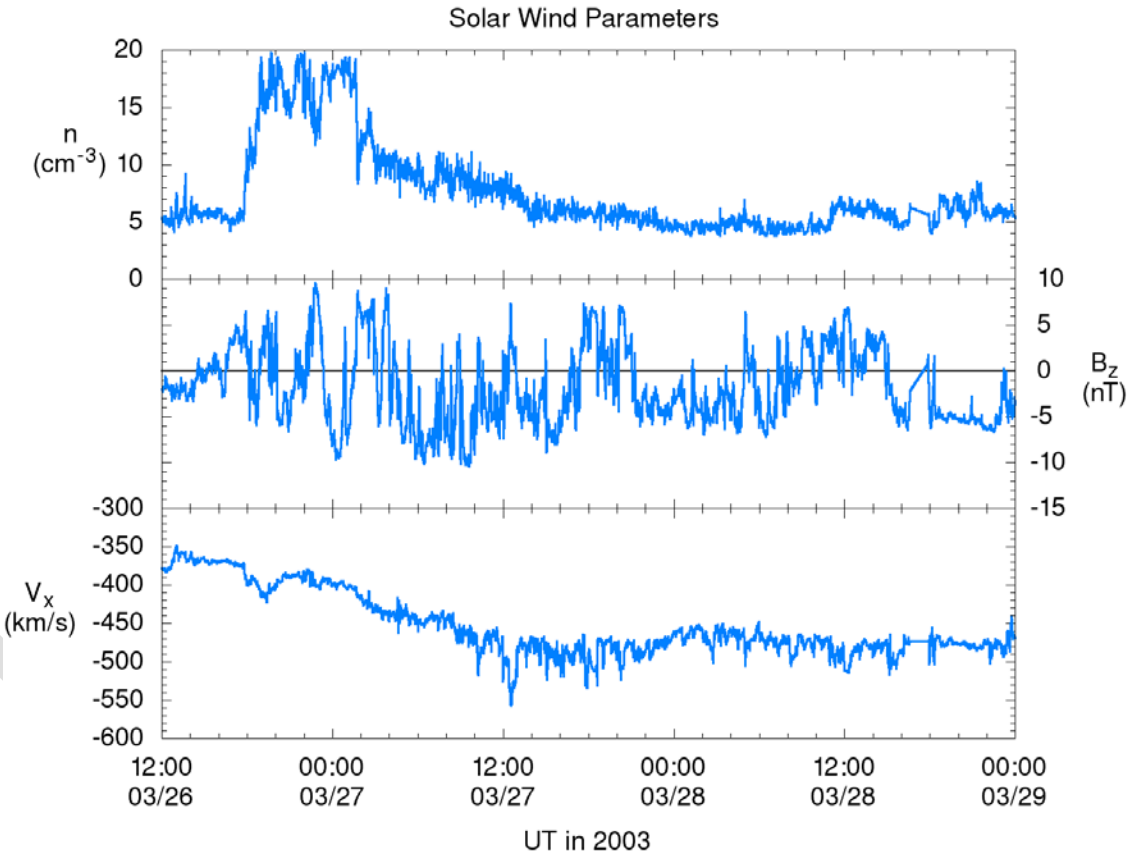


Figure S2. Solar wind density (n), Bz, and Vx profile for the March 26-28, 2003 stream interaction region obtained from CDAWeb. The other solar wind parameters (Vy, Vz, Bx, and By) were set to 0. All parameters are in SM-coordinates.

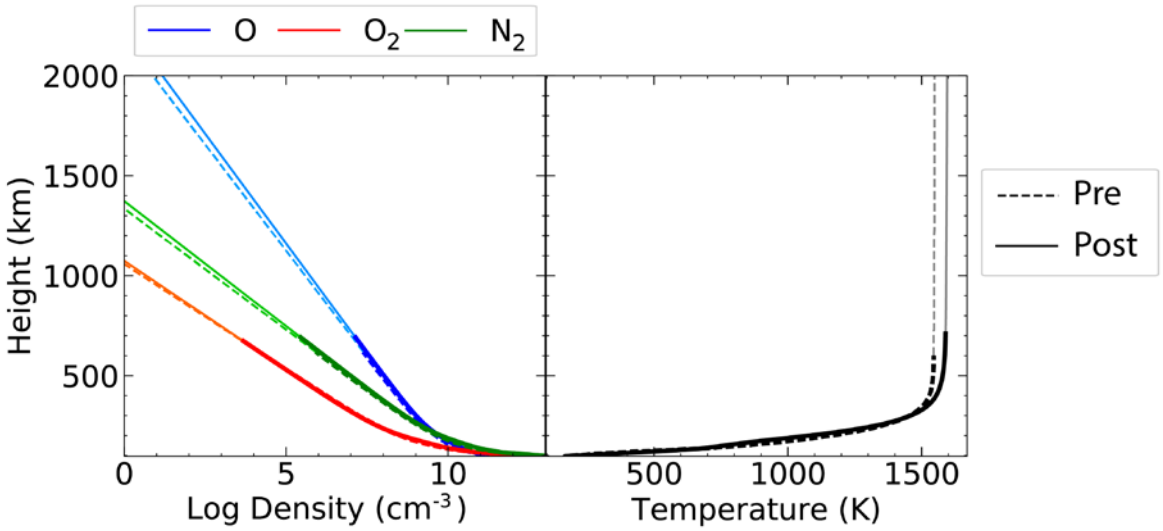


Figure S3. Altitude distribution of neutral density of O (blue), O2 (red), and N2 (green). Also profiles for neutral temperature (right). The distribution is split between pre-noon (dashed) and post-noon (solid) that correspond to the right (10 MLT) and left (14 MLT) magenta crosses in Figure 3.

In Review